E1, E2, M1, and M2 transitions in the nickel isoelectronic sequence

S.M. Hamasha, A.S. Shlyaptseva, and U.I. Safronova

Abstract: A relativistic many-body method is developed to calculate energy and transition rates for multipole transitions in many-electron ions. This method is based on relativistic many-body perturbation theory (RMBPT), agrees with MCDF calculations in lowest order, includes all second-order correlation corrections, and includes corrections from negative-energy states. Reduced matrix elements, oscillator strengths, and transition rates are calculated for electric-dipole (E1) and electric-quadrupole (E2) transitions, and magnetic-dipole (M1) and magnetic-quadrupole (M2) transitions in Ni-like ions with nuclear charges ranging from $Z = 30$ to 100. The calculations start from a $1s^22s^22p^63s^23p^63d^{10}$ Dirac–Fock potential. First-order perturbation theory is used to obtain intermediate-coupling coefficients, and second-order RMBPT is used to determine the matrix elements. The contributions from negative-energy states are included in the second-order E1, M1, E2, and M2 matrix elements. The resulting transition energies and transition rates are compared with experimental values and with results from other recent calculations.

PACS Nos.: 32.30.Rj, 32.70.Cs, 32.80.Rm, 34.70.+e

Résumé : Nous développons une méthode relativiste à N corps pour calculer l'énergie et les taux de transitions multiples dans les atomes multi-électroniques. Cette méthode, qui est basée sur la théorie perturbative relativiste (RMBPT), est en accord avec les calculs MCDF à l'ordre le plus bas, inclut toutes les corrections de corrélation du second ordre et les corrections pour les états d'énergie négative. Nous calculons les éléments de matrice réduits, les forces d'oscillateur et les taux de transition pour les transitions dipolaires électriques (E1), dipolaires magnétiques (M1), quadripolaires électriques (E2) et quadripolaires magnétiques (M2) dans les ions de type Ni avec charges nucléaires dans le domaine $Z = 30$–100. Le calcul démarre avec un potentiel Dirac–Fock $1s^22s^22p^63s^23p^63d^{10}$. Nous utilisons les perturbation au premier ordre pour obtenir les coefficients de couplage intermédiaire et au deuxième ordre RMBPT pour obtenir les éléments de matrice. Les contributions des états d'énergie négative sont inclues dans les éléments de matrice E1, M1, E2 et M2. Nous comparons nos énergies et taux de transition avec les résultats expérimentaux et avec les résultats calculés par d'autre sauteurs.

[Traduit par la Rédaction]

1. Introduction

Relativistic many-body perturbation theory (RMBPT) was used recently to study atomic characteristics of particle–hole excitations of closed-shell ions [1–6]. In the first of these studies, energies [1–3]

Received 25 November 2003. Accepted 4 February 2004. Published on the NRC Research Press Web site at http://cjp.nrc.ca/ on 14 May 2004.

S.M. Hamasha and A.S. Shlyaptseva.[1] Physics Department, University of Nevada, Reno, NV 89557, U.S.A.
U.I. Safronova. Department of Physics, University of Notre Dame, Notre Dame, IN 46566, U.S.A.

[1] Corresponding author (e-mail: alla@physics.unr.edu).

 doi: 10.1139/P04-007

and oscillator strengths [4] in Ne-like ions were considered by Avgoustoglou et al. Reduced matrix elements, oscillator strengths, and transition rates into the ground state for all allowed and forbidden electric- and magnetic-dipole and electric- and magnetic-quadrupole transitions (E1, M1, E2, M2) in Ne-like ions were presented by Safronova in ref. 5. The second-order RMBPT calculations for Ni-like ions was used in ref. 6 to determine excitation energies and oscillator strengths.

The Ni-isoelectronic sequence has been studied extensively in connection with X-ray lasers. The lasing action occurs because the $3d^{-1}4d$ levels are metastable to radiative decay to the Ni-like ground state; the transitions to the ground state from the lower $3d^{-1}4p$ levels are of course radiatively allowed. Ni-like X-ray lasers were first demonstrated in 1987 in a laser-produced plasma of Eu and later in laser-produced plasmas of Ta, W, and Au (see refs. 7 and 8 and references therein). Accurate knowledge of the lasing wavelengths is essential for applications to laboratory X-ray lasers. Wavelengths of $3d^9 4d\,{}^1S_0$–$3d^9 4p\,{}^1P_1$ X-ray lines in several low-Z Ni-like ions ranging from Y ($Z = 39$) to Cd ($Z = 48$) were measured recently by Li et al. [9]. Measurements for two lasing lines: $3d_{3/2}4d_{3/2}(0)$–$3d_{5/2}4p_{3/2}(1)$ and $3d_{3/2}4d_{3/2}(0)$–$3d_{5/2}4p_{1/2}(1)$ in ions ranging from Nd ($Z = 60$) to Ta ($Z = 73$) were reported by Daido et al. in ref. 10. It should be noted that neither LS nor jj coupling schemes described these states properly; this is why different designations are used for these states in refs. 9 and 10. Lasing on the Ni-like $3d^9 4f\,{}^1P_1$–$3d^9 4d\,{}^1P_1$ X-ray line in Zr ($Z = 40$), Nb ($Z = 41$), and Mo ($Z = 42$) are reported by Nilsen et al. in ref. 11. Measured wavelengths are presented for these ions as well as predicted values for ions from $Z = 36$ to 54. The predictions in ref. 11 were made by fitting the differences between energies calculated with the multiconfiguration Dirac–Fock (MCDF) code and experimentally determined energies for $Z = 37$ to 42 to a straight line. A similar method was used for predicting lasing lines in refs. 7 and 9. Accurate theoretical values for two lasing lines: $3d_{3/2}4d_{3/2}(0)$–$3d_{5/2}4p_{3/2}(1)$ and $3d_{3/2}4d_{3/2}(0)$–$3d_{5/2}4p_{1/2}(1)$ in selected Ni-like ions with Z from 60 to 73 were presented in ref. 10, where it was shown that good agreement between theoretical and experimental wavelengths could be obtained by taking into account the d-correlation.

A detailed analysis of 3–4 transitions in the X-ray spectrum by laser-produced plasmas of Ni-like Ba ($Z = 56$), La ($Z = 57$), and Pr ($Z = 59$) is reported by Doron et al. [12] and Zigler et al. [13]. Ab-initio calculations are reported in ref. 12 using the RELAC relativistic computer code to identify $3d - nf$ ($n = 4$ to 8), $3p - 4s$, and $3p - 4d$ transitions of Ni-like Ba. The same computer code was used by Busquet et al. [14] to identify X-ray spectral lines emitted by a target of Au ($Z = 79$). In ref. 14, a detailed description of the RELAC code, which is based on a relativistic model potential, is given. The HULLAC package is also based on a relativistic model potential [15]. The $n = 3$–4 transitions observed in X-ray spectra of Ni-like ions (Ag^{19+}–Pb^{54+}) were investigated theoretically by Quinet and Biémont [16], where the MCDF approach (Grant's code) was used to calculate wavelengths and oscillator strengths for the $3d - 4p$, $3d - 4f$, $3p - 4s$, and $3p - 4d$ electric-dipole transitions. The theoretical results in ref. 16 were compared with all previous published experimental data obtained from X-ray spectra emitted by strongly ionized atoms and generated by vacuum sparks, Tokamaks, or high-power lasers and the differences between theoretical and experimental values for the 3–4 transition were found to be about 0.5%. The relative magnitudes of the electric-multipole (E1, E2, E3) and magnetic-multipole (M1, M2, M3) radiative decay rates calculated by the MCDF approach, are presented by Biémont [17] for the lowest 17 levels of highly ionized nickel-like ions. Observation of electric-quadrupole and magnetic-octupole decay in the X-ray spectum of highly charged Ni-like ions (Th^{62+} and U^{64+}) are reported by Beiersdorfer et al. in ref. 18.

There are fewer papers concerned with the analysis of the $4s - 4p$ and $4p - 4d$ transitions in Ni-like ions. Spectra of 4–4 transitions in a laser-produced plasma of Ni-like ions (Ru^{16+}–Sn^{22+}) are observed and analyzed by Churilov et al. in ref. 19. The analysis of these spectra was based on the theoretical prediction by Wyart [20]. The prediction of $4s - 4p$ and $4p - 4d$ transitions in Ni-like ions (Mo^{14+}–Sn^{22+}) in ref. 20 was based on Slater–Condon type calculations of $3d^9 4s$, $3d^9 4p$, and $3d^9 4d$ configurations. The radial parameters involved in the three configurations were determined by

generalized least-squares fits using all known levels in the sequence.

In the present paper, relativistic many-body perturbation theory (RMBPT) is used to determine energies of the $3s^2 3p^6 3d^9 4l(J)$, $3s^2 3p^5 3d^{10} 4l(J)$, and $3s 3p^6 3d^{10} 4l(J)$ states of Ni-like ions with nuclear charges $Z = 30$–100. The calculations are carried out to second order in perturbation theory. The second-order RMBPT calculations for Ni-like ions start from a $1s^2 2s^2 2p^6 3s^2 3p^6 3d^{10}$ Dirac–Fock potential. Corrections for the frequency-dependent Breit interaction are included in first order only. Lamb-shift corrections to energies are also estimated and included. We consider all possible $3l$ holes and $4l$ particles leading to the 56 odd-parity $3d^{-1}4p(J)$, $3d^{-1}4f(J)$, $3p^{-1}4s(J)$, $3p^{-1}4d(J)$, $3s^{-1}4p(J)$, and $3s^{-1}4f(J)$ excited states and the 50 even-parity $3d^{-1}4s(J)$, $3d^{-1}4d(J)$, $3p^{-1}4p(J)$, $3p^{-1}4f(J)$, $3s^{-1}4s(J)$, and $3s^{-1}4d(J)$ excited states in Ni-like ions with $Z = 30$ to 100.

Relativistic MBPT is used to determine reduced matrix elements, oscillator strengths, and transition rates for all allowed and forbidden electric-dipole and magnetic-dipole (E1, M1) and electric-quadrupole and magnetic-quadrupole transitions (E2, M2) from $3s^2 3p^6 3d^9 4l(J)$, $3s^2 3p^5 3d^{10} 4l(J)$, and $3s 3p^6 3d^{10} 4l(J)$ excited states into the ground state in Ni-like ions. Retarded E1 and E2 matrix elements are evaluated in both length and velocity forms. The present RMBPT calculations start from a nonlocal $1s^2 2s^2 2p^6 3s^2 3p^6 3d^{10}$ Dirac–Fock potential and consequently give gauge-dependent transition matrix elements. Second-order correlation corrections compensate almost exactly for the gauge dependence of the first-order matrix elements, leading to corrected matrix elements that differ by less than 1% in length and velocity forms throughout the Ni isoelectronic sequence.

2. Theoretical technique

Details of the RMBPT method are presented in refs. 1 and 6 for the calculation of energies of hole–particle states, in ref. 21 for the calculation of energies of particle–particle states, in ref. 22 for the calculation of radiative electric-dipole rates in two-particle states, and in ref. 5 for calculation of multipole radiative rates in Ne-like system. We will present, here, only the model space for Ni-like ions and the first- and second-order diagram contributions for hole–particle systems without repeating the detailed discussions given in refs. 1, 6, 21, 22, and 5.

For atoms with one hole in closed shells and one electron above the closed shells, the model space is formed from hole–particle states of the type $a_v^+ a_a|0\rangle$, where $|0\rangle$ is the closed-shell and the ground state is $1s^2_{1/2} 2s^2_{1/2} 2p^2_{1/2} 2p^4_{3/2}\ 3s^2_{1/2} 3p^2_{1/2} 3p^4_{3/2}\ 3d^4_{3/2} 3d^6_{3/2}$. The single-particle indices v range over states in the valence shell and the single-hole indices a range over the closed core. For our study of low-lying states $3l^{-1}4l'$ states of Ni-like ions, values of a are $3s_{1/2}$, $3p_{1/2}$, $3p_{3/2}$, $3d_{3/2}$, and $3d_{5/2}$, while values of v are $4s_{1/2}$, $4p_{1/2}$, $4p_{3/2}$, $4d_{3/2}$, $4d_{5/2}$, $4f_{5/2}$, and $4f_{7/2}$. To obtain orthonormal model states, we consider the coupled states $\Phi_{JM}(av)$ defined by

$$\Phi_{JM}(av) = \sqrt{(2J+1)} \sum_{m_a m_v} (-1)^{j_v - m_v} \begin{pmatrix} j_v & J & j_a \\ -m_v & M & m_a \end{pmatrix} a^\dagger_{vm_v} a_{am_a}|0\rangle \tag{1}$$

Combining the $n = 3$ hole orbitals and the $n = 4$ particle orbitals in nickel, we obtain 56 odd-parity states consisting of five $J = 0$ states, thirteen $J = 1$ states, fifteen $J = 2$ states, twelve $J = 3$ states, seven $J = 4$ states, three $J = 5$ states, and one $J = 6$ state. Additionally, there are 50 even-parity states consisting of five $J = 0$ states, twelve $J = 1$ states, fourteen $J = 2$ states, eleven $J = 3$ states, six $J = 4$ states, and two $J = 5$ states. The distribution of the 106 states in the model space is summarized in Table 1. In Table 1, we give both jj and LS designations for hole–particle states and instead of using the $3l_j^{-1}4l'_{j'}$ or $3l^{-1}4l'$ designations, we use simpler designations $3l_j 4l'_{j'}$ or $3l4l'$. The same ($3l_j 4l'_{j'}$ or $3l4l'$) designations are used for simplicity in all the following tables and the text below.

Analytical expressions for energy matrixes and multipole matrix elements in the second-order RMBPT are given by (2.2)–(2.11) and (2.12)–(2.17), respectively, in ref. 6. Electric- and magnetic-dipole and electric- and magnetic-quadrupole first-order matrix elements together with derivative terms are presented in the Appendix.

Table 1. Possible hole–particle states in the $3lj4l'j'(J)$ and $3l4l'LS$ complexes; jj and LS coupling schemes.

Odd-parity states

jj coupl.	LS coupl.	jj coupl.	LS coupl.	jj coupl.	LS coupl.	jj coupl.	LS coupl.
$3d_{3/2}4p_{3/2}(0)$	$3d4p\,^3P$	$3d_{3/2}4p_{1/2}(1)$	$3d4p\,^3P$	$3d_{5/2}4p_{1/2}(2)$	$3d4p\,^3F$	$3d_{5/2}4p_{1/2}(3)$	$3d4p\,^3F$
$3d_{5/2}4f_{5/2}(0)$	$3d4f\,^3P$	$3d_{5/2}4p_{3/2}(1)$	$3d4p\,^3D$	$3d_{5/2}4p_{3/2}(2)$	$3d4p\,^3P$	$3d_{5/2}4p_{3/2}(3)$	$3d4p\,^1F$
$3p_{1/2}4s_{1/2}(0)$	$3p4s\,^3P$	$3d_{3/2}4p_{3/2}(1)$	$3d4p\,^1P$	$3d_{3/2}4p_{1/2}(2)$	$3d4p\,^1D$	$3d_{3/2}4p_{3/2}(3)$	$3d4p\,^3D$
$3p_{3/2}4d_{3/2}(0)$	$3p4d\,^3P$	$3d_{5/2}4f_{5/2}(1)$	$3d4f\,^3P$	$3d_{3/2}4p_{3/2}(2)$	$3d4p\,^3D$	$3d_{5/2}4f_{5/2}(3)$	$3d4f\,^3D$
$3s_{1/2}4p_{1/2}(0)$	$3s4p\,^3P$	$3d_{5/2}4f_{7/2}(1)$	$3d4f\,^3D$	$3d_{5/2}4f_{5/2}(2)$	$3d4f\,^3P$	$3d_{5/2}4f_{7/2}(3)$	$3d4f\,^3G$
$3d_{5/2}4p_{3/2}(4)$	$3d4p\,^3F$	$3d_{3/2}4f_{5/2}(1)$	$3d4f\,^1P$	$3d_{5/2}4f_{7/2}(2)$	$3d4f\,^3D$	$3d_{3/2}4f_{5/2}(3)$	$3d4f\,^3F$
$3d_{5/2}4f_{5/2}(4)$	$3d4f\,^3H$	$3p_{3/2}4s_{1/2}(1)$	$3p4s\,^1P$	$3d_{3/2}4f_{5/2}(2)$	$3d4f\,^1D$	$3d_{3/2}4f_{7/2}(3)$	$3d4f\,^1F$
$3d_{5/2}4f_{7/2}(4)$	$3d4f\,^3G$	$3p_{1/2}4s_{1/2}(1)$	$3p4s\,^3P$	$3d_{3/2}4f_{7/2}(2)$	$3d4f\,^3F$	$3p_{3/2}4d_{3/2}(3)$	$3p4d\,^3F$
$3d_{3/2}4f_{5/2}(4)$	$3d4f\,^3F$	$3p_{3/2}4d_{3/2}(1)$	$3p4d\,^3P$	$3p_{3/2}4s_{1/2}(2)$	$3p4s\,^3P$	$3p_{3/2}4d_{5/2}(3)$	$3p4d\,^1F$
$3d_{3/2}4f_{7/2}(4)$	$3d4f\,^1G$	$3p_{3/2}4d_{5/2}(1)$	$3p4d\,^1P$	$3p_{3/2}4d_{3/2}(2)$	$3p4d\,^3F$	$3p_{1/2}4d_{5/2}(3)$	$3p4d\,^3D$
$3p_{3/2}4d_{5/2}(4)$	$3p4d\,^3F$	$3p_{1/2}4d_{3/2}(1)$	$3p4d\,^3D$	$3p_{3/2}4d_{5/2}(2)$	$3p4d\,^3P$	$3s_{1/2}4f_{5/2}(3)$	$3s4f\,^3F$
$3s_{1/2}4f_{7/2}(4)$	$3s4f\,^3F$	$3s_{1/2}4p_{1/2}(1)$	$3s4p\,^3P$	$3p_{1/2}4d_{3/2}(2)$	$3p4d\,^3D$	$3s_{1/2}4f_{7/2}(3)$	$3s4f\,^1F$
$3d_{5/2}4f_{5/2}(5)$	$3d4f\,^3H$	$3s_{1/2}4p_{3/2}(1)$	$3s4p\,^1P$	$3p_{1/2}4d_{5/2}(2)$	$3p4d\,^1D$		
$3d_{5/2}4f_{7/2}(5)$	$3d4f\,^3G$			$3s_{1/2}4p_{3/2}(2)$	$3s4p\,^3P$		
$3d_{3/2}4f_{7/2}(5)$	$3d4f\,^1H$			$3s_{1/2}4f_{5/2}(2)$	$3s4f\,^3F$		
$3d_{5/2}4f_{7/2}(6)$	$3d4f\,^3H$						

Even-parity states

jj coupl.	LS coupl.	jj coupl.	LS coupl.	jj coupl.	LS coupl.	jj coupl.	LS coupl.
$3d_{5/2}4d_{5/2}(0)$	$3d4d\,^3P$	$3d_{3/2}4s_{1/2}(1)$	$3d4s\,^3D$	$3d_{5/2}4s_{1/2}(2)$	$3d4s\,^3D$	$3d_{5/2}4s_{1/2}(3)$	$3d4s\,^3D$
$3d_{3/2}4d_{3/2}(0)$	$3d4d\,^1S$	$3d_{5/2}4d_{3/2}(1)$	$3d4d\,^3S$	$3d_{3/2}4s_{1/2}(2)$	$3d4s\,^1D$	$3d_{5/2}4d_{3/2}(3)$	$3d4d\,^3G$
$3p_{3/2}4p_{3/2}(0)$	$3p4p\,^3P$	$3d_{5/2}4d_{5/2}(1)$	$3d4d\,^1P$	$3d_{5/2}4d_{3/2}(2)$	$3d4d\,^3P$	$3d_{5/2}4d_{5/2}(3)$	$3d4d\,^3D$
$3p_{1/2}4p_{1/2}(0)$	$3p4p\,^1S$	$3d_{3/2}4d_{3/2}(1)$	$3d4d\,^3D$	$3d_{5/2}4d_{5/2}(2)$	$3d4d\,^3D$	$3d_{3/2}4d_{3/2}(3)$	$3d4d\,^3F$
$3s_{1/2}4s_{1/2}(0)$	$3s4s\,^1S$	$3d_{3/2}4d_{5/2}(1)$	$3d4d\,^3P$	$3d_{3/2}4d_{3/2}(2)$	$3d4d\,^3F$	$3d_{3/2}4d_{5/2}(3)$	$3d4d\,^1F$
$3d_{5/2}4d_{3/2}(4)$	$3d4d\,^3G$	$3p_{3/2}4p_{1/2}(1)$	$3p4p\,^3D$	$3d_{3/2}4d_{5/2}(2)$	$3d4d\,^1D$	$3p_{3/2}4p_{3/2}(3)$	$3p4p\,^3D$
$3d_{5/2}4d_{5/2}(4)$	$3d4d\,^1G$	$3p_{3/2}4p_{3/2}(1)$	$3p4p\,^3S$	$3p_{3/2}4p_{1/2}(2)$	$3p4p\,^3D$	$3p_{3/2}4f_{5/2}(3)$	$3p4f\,^3D$
$3d_{3/2}4d_{5/2}(4)$	$3d4d\,^3F$	$3p_{1/2}4p_{1/2}(1)$	$3p4p\,^1P$	$3p_{3/2}4p_{3/2}(2)$	$3p4p\,^1D$	$3p_{1/2}4f_{5/2}(3)$	$3p4f\,^3G$
$3p_{3/2}4f_{5/2}(4)$	$3p4f\,^3G$	$3p_{1/2}4p_{3/2}(1)$	$3p4p\,^3P$	$3p_{1/2}4p_{3/2}(2)$	$3p4p\,^3P$	$3p_{3/2}4f_{7/2}(3)$	$3p4f\,^1F$
$3p_{3/2}4f_{7/2}(4)$	$3p4f\,^1G$	$3p_{3/2}4f_{5/2}(1)$	$3p4f\,^3D$	$3p_{3/2}4f_{5/2}(2)$	$3p4f\,^3D$	$3p_{1/2}4f_{7/2}(3)$	$3p4f\,^3F$
$3p_{1/2}4f_{7/2}(4)$	$3p4f\,^3F$	$3s_{1/2}4s_{1/2}(1)$	$3s4s\,^3S$	$3p_{3/2}4f_{7/2}(2)$	$3p4f\,^1D$	$3s_{1/2}4d_{5/2}(3)$	$3s4d\,^3D$
$3d_{5/2}4d_{5/2}(5)$	$3p4f\,^3G$	$3s_{1/2}4d_{3/2}(1)$	$3s4d\,^3D$	$3p_{1/2}4f_{5/2}(2)$	$3p4f\,^3F$		
$3p_{3/2}4f_{7/2}(5)$	$3p4f\,^3G$			$3s_{1/2}4d_{3/2}(2)$	$3s4d\,^3D$		
				$3s_{1/2}4d_{5/2}(2)$	$3s4d\,^1D$		

3. Excitation energies

3.1. Example: energy matrix for W^{46+}

In Table 2, we give various contributions to the second-order energies for the special case of Ni-like tungsten, $Z = 74$. In Table 2, we show the one-body and two-body second-order Coulomb contributions to the energy matrix labeled $E_1^{(2)}$ and $E_2^{(2)}$, respectively. The corresponding Breit–Coulomb contributions are given in columns headed $B_1^{(2)}$ and $B_2^{(2)}$. The one-body second-order energy is obtained as a sum of the valence $E_v^{(2)}$ and hole $E_a^{(2)}$ energies with the latter being the dominant contribution. The values of $E_1^{(2)}$ and $B_1^{(2)}$ are nonzero only for diagonal matrix elements. Although there are 106 diagonal and 1042 nondiagonal matrix elements for $(3l_j4l'_{j'})(J)$ hole–particle states, we list only part of the

Table 2. Second-order contributions to the energy matrices (a.u.) for odd-parity states with $J = 2$ in the case of Ni-like tungsten, $Z = 74$. One-body and two-body second-order Coulomb and Breit–Coulomb contributions are given in columns labeled $E_1^{(2)}$, $E_2^{(2)}$, $B_1^{(2)}$, and $B_2^{(2)}$, respectively.

		Coulomb interaction		Breit–Coulomb correction	
$3l_1j_1\,4l_2j_2$,	$3l_3j_3\,4l_4j_4$	$E_1^{(2)}$	$E_2^{(2)}$	$B_1^{(2)}$	$B_2^{(2)}$
$3d_{5/2}4p_{1/2}$	$3d_{5/2}4p_{1/2}$	−0.165064	0.061571	0.054106	0.004770
$3d_{5/2}4p_{3/2}$	$3d_{5/2}4p_{3/2}$	−0.154592	0.051703	0.055966	0.003453
$3d_{3/2}4p_{1/2}$	$3d_{3/2}4p_{1/2}$	−0.176234	0.063549	0.056644	0.004810
$3d_{3/2}4p_{3/2}$	$3d_{3/2}4p_{3/2}$	−0.165763	0.052947	0.058504	0.003570
$3d_{5/2}4f_{5/2}$	$3d_{5/2}4f_{5/2}$	−0.157878	0.043947	0.060093	0.002957
$3d_{5/2}4f_{7/2}$	$3d_{5/2}4f_{7/2}$	−0.154863	0.039527	0.060825	0.001999
$3d_{3/2}4f_{5/2}$	$3d_{3/2}4f_{5/2}$	−0.169049	0.043242	0.062631	0.002739
$3d_{3/2}4f_{7/2}$	$3d_{3/2}4f_{7/2}$	−0.166034	0.043219	0.063364	0.002031
$3p_{3/2}4s_{1/2}$	$3p_{3/2}4s_{1/2}$	−0.239748	0.045008	0.048713	0.003117
$3p_{3/2}4d_{3/2}$	$3p_{3/2}4d_{3/2}$	−0.243322	0.046631	0.046497	0.003430
$3p_{3/2}4d_{5/2}$	$3p_{3/2}4d_{5/2}$	−0.239194	0.044062	0.046897	0.002790
$3p_{1/2}4d_{3/2}$	$3p_{1/2}4d_{3/2}$	−0.293196	0.059744	0.053373	0.004037
$3p_{1/2}4d_{5/2}$	$3p_{1/2}4d_{5/2}$	−0.289068	0.067060	0.053773	0.003396
$3s_{1/2}4p_{3/2}$	$3s_{1/2}4p_{3/2}$	−0.301835	0.037263	0.047780	0.003076
$3s_{1/2}4f_{5/2}$	$3s_{1/2}4f_{5/2}$	−0.305121	−0.004315	0.051907	0.003058
$3d_{5/2}4p_{1/2}$	$3d_{5/2}4p_{3/2}$		−0.003176		−0.000175
$3d_{5/2}4p_{3/2}$	$3d_{5/2}4p_{1/2}$		−0.002828		−0.000194
$3d_{5/2}4p_{1/2}$	$3d_{3/2}4p_{1/2}$		0.000346		−0.000045
$3d_{3/2}4p_{1/2}$	$3d_{5/2}4p_{1/2}$		0.000365		0.000051
$3d_{5/2}4p_{1/2}$	$3d_{3/2}4p_{3/2}$		0.001105		0.000103
$3d_{3/2}4p_{3/2}$	$3d_{5/2}4p_{1/2}$		0.000745		0.000181
$3d_{5/2}4p_{1/2}$	$3d_{5/2}4f_{5/2}$		0.002992		0.000161
$3d_{5/2}4f_{5/2}$	$3d_{5/2}4p_{1/2}$		0.003058		0.000218
$3d_{5/2}4p_{1/2}$	$3d_{5/2}4f_{7/2}$		0.000901		0.000135
$3d_{5/2}4f_{7/2}$	$3d_{5/2}4p_{1/2}$		0.000851		0.000199

odd-parity subset with $J = 2$ in Table 2. It can be seen from Table 2 that second-order Breit–Coulomb corrections are relatively large and, therefore, must be included for accurate calculations. The values of the nondiagonal matrix elements given in columns headed $E_2^{(2)}$ and $B_2^{(2)}$ are comparable with the values of diagonal two-body matrix elements. However, the values of the one-body contributions, $E_1^{(2)}$ and $B_1^{(2)}$, are larger than the values of the two-body contributions, $E_2^{(2)}$ and $B_2^{(2)}$, respectively. As a result, total second-order diagonal matrix elements are much larger than the nondiagonal matrix elements that are shown in Table 3.

In Table 3, we present results for the zeroth-, first-, and second-order Coulomb contributions, $E^{(0)}$, $E^{(1)}$, and $E^{(2)}$, and the first- and second-order Breit–Coulomb corrections, $B_{\rm hf}^{(1)}$ and $B^{(2)}$. It should be noted that corrections for the frequency-dependent Breit interaction [23] are included in the first order only. The difference between the first-order Breit–Coulomb corrections calculated with and without frequency dependence is less than 1%. As one can see from Table 3, the ratio of nondiagonal and diagonal matrix elements is larger for the first-order contributions than for the second-order contributions. Another difference in the first- and second-order contributions is the symmetry properties: the first-order nondiagonal matrix elements are symmetric and the second-order nondiagonal matrix elements are not symmetric. The values of $E^{(2)}[a'v'(J), av(J)]$ and $E^{(2)}[av(J), a'v'(J)]$ matrix elements differ in some cases by a factor 2–3 and occasionally have opposite signs.

Table 3. Contributions to the energy matrix $E[3l_1j_1\,4l_2j_2(J), 3l_3j_3\,4l_4j_4(J)] = E^{(0)} + E^{(1)} + E^{(2)} + B^{(1)}_{hf} + B^{(2)}$ before diagonalization. These contributions are given for a hole–particle ion with a $1s^22s^22p^63s^23p^63d^{10}$ core, in the case of odd-parity states with $J = 2$, and $Z = 74$.

$3l_1j_1\,4l_2j_2$,	$3l_3j_3\,4l_4j_4$	$E^{(0)}$	$E^{(1)}$	$B^{(1)}_{\rm hf}$	$E^{(2)}$	$B^{(2)}$
$3d_{5/2}4p_{1/2}$	$3d_{5/2}4p_{1/2}$	63.946959	−2.897065	−0.044328	−0.103493	0.058876
$3d_{5/2}4p_{3/2}$	$3d_{5/2}4p_{3/2}$	67.700562	−2.766233	−0.086067	−0.102890	0.059419
$3d_{3/2}4p_{1/2}$	$3d_{3/2}4p_{1/2}$	66.454528	−2.910600	−0.101760	−0.112686	0.061454
$3d_{3/2}4p_{3/2}$	$3d_{3/2}4p_{3/2}$	70.208131	−2.701466	−0.137045	−0.112816	0.062074
$3d_{5/2}4f_{5/2}$	$3d_{5/2}4f_{5/2}$	80.001175	−3.040893	−0.131847	−0.113931	0.063050
$3d_{5/2}4f_{7/2}$	$3d_{5/2}4f_{7/2}$	80.210728	−3.102061	−0.147633	−0.115336	0.062824
$3d_{3/2}4f_{5/2}$	$3d_{3/2}4f_{5/2}$	82.508744	−3.027474	−0.189739	−0.125807	0.065370
$3d_{3/2}4f_{7/2}$	$3d_{3/2}4f_{7/2}$	82.718297	−3.185489	−0.197412	−0.122815	0.065395
$3p_{3/2}4s_{1/2}$	$3p_{3/2}4s_{1/2}$	76.989075	−2.802900	−0.185291	−0.194740	0.051830
$3p_{3/2}4d_{3/2}$	$3p_{3/2}4d_{3/2}$	89.908848	−2.712244	−0.199086	−0.196691	0.049927
$3p_{3/2}4d_{5/2}$	$3p_{3/2}4d_{5/2}$	90.715573	−2.770880	−0.216900	−0.195132	0.049688
$3p_{1/2}4d_{3/2}$	$3p_{1/2}4d_{3/2}$	101.409027	−2.862060	−0.326498	−0.233452	0.057411
$3p_{1/2}4d_{5/2}$	$3p_{1/2}4d_{5/2}$	102.215752	−2.831900	−0.339351	−0.222007	0.057169
$3s_{1/2}4p_{3/2}$	$3s_{1/2}4p_{3/2}$	104.600025	−2.736867	−0.175038	−0.264572	0.050856
$3s_{1/2}4f_{5/2}$	$3s_{1/2}4f_{5/2}$	116.900638	−3.011717	−0.223007	−0.309436	0.054964
$3d_{5/2}4p_{1/2}$	$3d_{5/2}4p_{3/2}$	0.000000	−0.141135	0.000847	−0.003176	−0.000175
$3d_{5/2}4p_{3/2}$	$3d_{5/2}4p_{1/2}$	0.000000	−0.141135	0.000847	−0.002828	−0.000194
$3d_{5/2}4p_{1/2}$	$3d_{3/2}4p_{1/2}$	0.000000	0.000000	0.000422	0.000346	−0.000045
$3d_{3/2}4p_{1/2}$	$3d_{5/2}4p_{1/2}$	0.000000	0.000000	0.000422	0.000365	0.000051
$3d_{5/2}4p_{1/2}$	$3d_{3/2}4p_{3/2}$	0.000000	−0.079629	−0.000306	0.001105	0.000103
$3d_{3/2}4p_{3/2}$	$3d_{5/2}4p_{1/2}$	0.000000	−0.079629	−0.000306	0.000745	0.000181
$3d_{5/2}4p_{1/2}$	$3d_{5/2}4f_{5/2}$	0.000000	−0.040667	0.000165	0.002992	0.000161
$3d_{5/2}4f_{5/2}$	$3d_{5/2}4p_{1/2}$	0.000000	−0.040667	0.000165	0.003058	0.000218
$3d_{5/2}4p_{1/2}$	$3d_{5/2}4f_{7/2}$	0.000000	0.008608	0.000737	0.000901	0.000135
$3d_{5/2}4f_{7/2}$	$3d_{5/2}4p_{1/2}$	0.000000	0.008608	0.000737	0.000851	0.000199

We now discuss how the final energy levels are obtained from the above contributions. To determine the first-order energies of the states under consideration, we diagonalize the symmetric first-order effective Hamiltonian, including both the Coulomb and Breit interactions. The first-order expansion coefficient $C^N[av(J)]$ is the Nth eigenvector of the first-order effective Hamiltonian and $E^{(1)}[N]$ is the corresponding eigenvalue. The resulting eigenvectors are used to determine the second-order Coulomb correction $E^{(2)}[N]$, the second-order Breit–Coulomb correction $B^{(2)}[N]$ and the QED correction $E_{\rm Lamb}[N]$.

In Table 4, we list the following contributions to the energies of 15 excited states in W^{46+}: the sum of the zeroth- and first-order energies $E^{(0+1)} = E^{(0)} + E^{(1)} + B^{(1)}_{\rm hf}$, the second-order Coulomb energy $E^{(2)}$, the second-order Breit–Coulomb correction $B^{(2)}$, the QED correction $E_{\rm Lamb}$, and the sum of the above contributions $E_{\rm tot}$. The QED correction is approximated as the sum of the one-electron self energy and the first-order vacuum-polarization energy. The screened self-energy and vacuum polarization data given by Kim et al. [24], which are in close agreement with screened self-energy calculations by Blundell [25], are used to determine the QED correction $E_{\rm Lamb}$.

When starting calculations from relativistic DHF wave functions, it is natural to use jj designations for uncoupled transition and energy matrix elements; however, neither jj nor LS coupling describes the physical states properly, except for the single-configuration state $3d_{5/2}4f_{7/2}(6) \equiv 3d4f\ ^3H_6$. Both designations are used in Table 4.

Table 4. Energies of Ni-like tungsten for odd-parity states with $J = 2$ relative to the ground state. $E^{(0+1)} \equiv E^{(0)} + E^{(1)} + B^{(1)}_{\rm hf}$.

jj coupl.	LS coupl.	$E^{(0+1)}$	$E^{(2)}$	$B^{(2)}$	$E_{\rm Lamb}$	$E_{\rm tot}$
$3d_{5/2}4p_{1/2}$	$3d4p\,^3F$	60.984569	−0.105568	0.058819	−0.000536	60.937284
$3d_{5/2}4p_{3/2}$	$3d4p\,^3P$	63.431374	−0.110837	0.061363	0.007112	63.389012
$3d_{3/2}4p_{1/2}$	$3d4p\,^1D$	64.835220	−0.100670	0.059479	0.003707	64.797735
$3d_{3/2}4p_{3/2}$	$3d4p\,^3D$	67.361256	−0.112172	0.061944	0.011364	67.322393
$3d_{5/2}4f_{5/2}$	$3d4f\,^3P$	74.038405	−0.193298	0.051893	0.027450	73.924449
$3d_{5/2}4f_{7/2}$	$3d4f\,^3D$	76.790414	−0.114212	0.063027	−0.004421	76.734808
$3d_{3/2}4f_{5/2}$	$3d4f\,^1D$	76.973652	−0.112346	0.062906	−0.003648	76.920563
$3d_{3/2}4f_{7/2}$	$3d4f\,^3F$	79.249794	−0.123899	0.065239	0.003390	79.194524
$3p_{3/2}4s_{1/2}$	$3p4s\,^3P$	79.376078	−0.123261	0.065484	0.003877	79.322178
$3p_{3/2}4d_{3/2}$	$3p4d\,^3F$	87.017623	−0.198179	0.049910	−0.027362	86.841992
$3p_{3/2}4d_{5/2}$	$3p4d\,^3P$	87.747648	−0.194982	0.049711	−0.025308	87.577069
$3p_{1/2}4d_{3/2}$	$3p4d\,^3D$	98.221187	−0.236010	0.057493	−0.013794	98.028875
$3p_{1/2}4d_{5/2}$	$3p4d\,^1D$	98.996485	−0.235425	0.056976	−0.014971	98.803064
$3s_{1/2}4p_{3/2}$	$3s4p\,^3P$	101.761043	−0.256048	0.051078	−0.159746	101.396327
$3s_{1/2}4f_{5/2}$	$3s4f\,^3F$	113.672635	−0.308896	0.054984	−0.171642	113.247081

3.2. *Z* dependence of eigenvectors and eigenvalues in Ni-like ions

In Figs. 1 and 2, we illustrate the Z dependence of the eigenvectors and eigenvalues of the $3l_j\,4l'_{j'}\,(J)$ hole–particle states. Strong mixing between states within odd-parity complex with $J = 1$ was discussed in many papers (see, for example, ref. 6). We refer to a set of states of the same parity and the same J as a complex of states. Additionally, we found strong mixing within the odd-parity complex with $J = 2$ and even-parity complex with $J = 1$, and 2. In Fig. 1, we show the dependence of the eigenvectors for the example of even-parity states with $J = 2$. This particular $J = 2$ even-parity complex includes 14 states that are listed in Table 1. Using the first-order expansion coefficients $C^N[av(J)]$ defined in the previous section, we can present the resulting eigenvectors as

$$\begin{aligned}\Phi(N) \;=\;& C^N[3d_{5/2}4s_{1/2}(2)]\Phi[3d_{5/2}4s_{1/2}(2)] + C^N[3d_{3/2}4s_{1/2}(2)]\Phi[3d_{3/2}4s_{1/2}(2)] + \\ & C^N[3d_{5/2}4d_{3/2}(2)]\Phi[3d_{5/2}4d_{3/2}(2)] + C^N[3d_{5/2}4d_{5/2}(2)]\Phi[3d_{5/2}4d_{5/2}(2)] + \\ & C^N[3d_{3/2}4d_{3/2}(2)]\Phi[3d_{3/2}4d_{3/2}(2)] + C^N[3d_{3/2}4d_{5/2}(2)]\Phi[3d_{3/2}4d_{5/2}(2)] + \\ & C^N[3p_{3/2}4p_{1/2}(2)]\Phi[3p_{3/2}4p_{1/2}(2)] + C^N[3p_{3/2}4p_{3/2}(2)]\Phi[3p_{3/2}4p_{3/2}(2)] + \\ & C^N[3p_{1/2}4p_{3/2}(2)]\Phi[3p_{1/2}4p_{3/2}(2)] + C^N[3p_{3/2}4f_{5/2}(2)]\Phi[3p_{3/2}4f_{5/2}(2)] + \\ & C^N[3p_{3/2}4f_{7/2}(2)]\Phi[3p_{3/2}4f_{7/2}(2)] + C^N[3p_{1/2}4f_{5/2}(2)]\Phi[3p_{1/2}4f_{5/2}(2)] + \\ & C^N[3s_{1/2}4d_{3/2}(2)]\Phi[3s_{1/2}4d_{3/2}(2)] + C^N[3s_{1/2}4d_{5/2}(2)]\Phi[3s_{1/2}4d_{5/2}(2)] \qquad (2)\end{aligned}$$

As a result, $196C^N[av(J)]$ coefficients are needed to describe the 14 eigenvalues. These coefficients are often called mixing coefficients. For simplicity, we plot only three of the 14 mixing coefficients for the level $N = 3p4f\,^3D_2$ in Fig. 1. These coefficients are chosen to illustrate the mixing of the states; the remaining mixing coefficients give very small contributions to this level. We observe strong mixing between $[3p_{3/2}4f_{5/2}(2)] + [3p_{1/2}4f_{7/2}(2)] + [3p_{1/2}4p_{3/2}(2)]$ states for $Z = 41$–42 and $Z = 75$–76.

Energies, relative to the ground state, of even-parity states with $J = 1$ and 2, divided by $(Z - 21)^2$, are shown in Fig. 2. It should be noted that Z was decreased by 21 to provide better presentation of the energy diagrams. We plot the limited number of energy levels to illustrate Z dependence choosing one representative from a configuration. As a result, we show 6 levels instead of 12 in Fig. 2*a*, and 5 levels instead of 14 in Fig. 2*b*. It should be noted that the LS designations are chosen by comparing our results

Fig. 1. Mixing coefficients for the $3p4f\,^3D_2$ level as functions of Z.

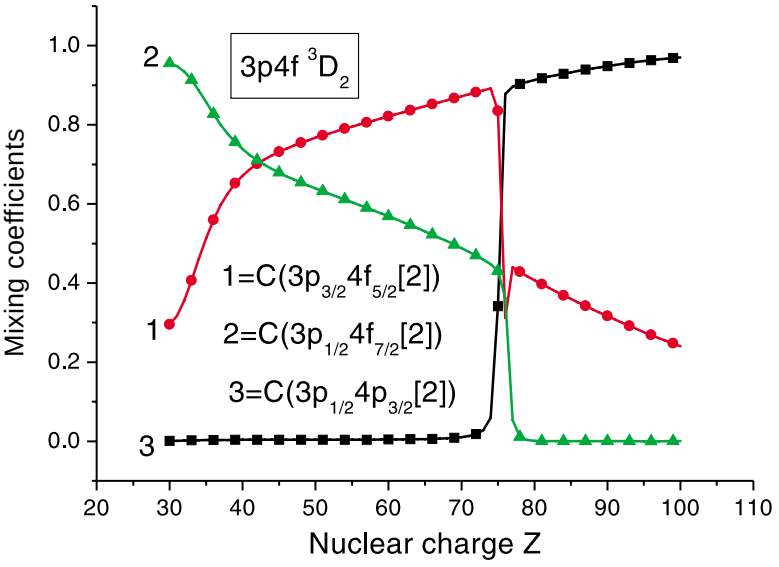

Fig. 2. Energies $(E/(Z-21)^2)$ in cm^{-1} for even-parity states with $J = 1$ and 2 in Ni-like ions as function of Z.

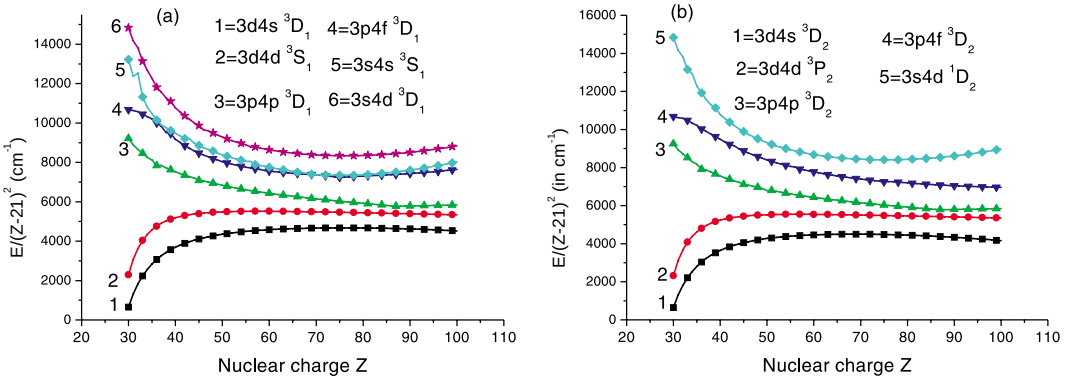

with available experimental data for low-Z ions. To confirm those LS designations we obtain the fine structure splitting for the $3d4s$, $3d4d$, $3p4p$, $3p4f$, $3s4s$, and $3s4d$ triplets.

Energy differences between levels of even-parity triplet terms, divided by $(Z-21)^2$, are shown in Fig. 3. In Fig. 3, we show how the energy intervals vary strongly with nuclear charge for the ^3D term of $3d4s$ configuration, ^3P, ^3D, ^3F, and ^3G terms of $3d4d$ configuration, and ^3P, ^3D terms of $3p4p$ configuration. Our calculations show that the fine structures of the $3d4s$, $3d4d$, and $3p4p$ levels do not follow the Landé rules even for small Z. As can be seen from Fig. 3*a*, the $3d4s\,^3D$ levels are completely inverted, the $3d4s$ ($^3D_3 - ^3D_2$) interval changes very slowly with Z, while the $3d4s$ ($^3D_2 - ^3D_1$) interval increases by factor 25 in the range of $Z = 30$–100. The $3d4d\,^3D$ levels (Fig. 3*c*) are also completely inverted, while $3d4d\,^3P$, ^3F, ^3G levels are partially inverted and only the $3p4p\,^3P$, ^3D levels (Fig. 3*b*) show regular ordering of the fine-structure splittings for low and high Z. The unusual splittings are principally due to changes from LS to jj coupling, with mixing from other triplet and singlet states. The different J states are mixed differently. Further experimental confirmation would be

Fig. 3. Energy splitting ($\Delta E/(Z-21)^2$) in cm^{-1} for terms of even-parity states in Ni-like ions as function of Z.

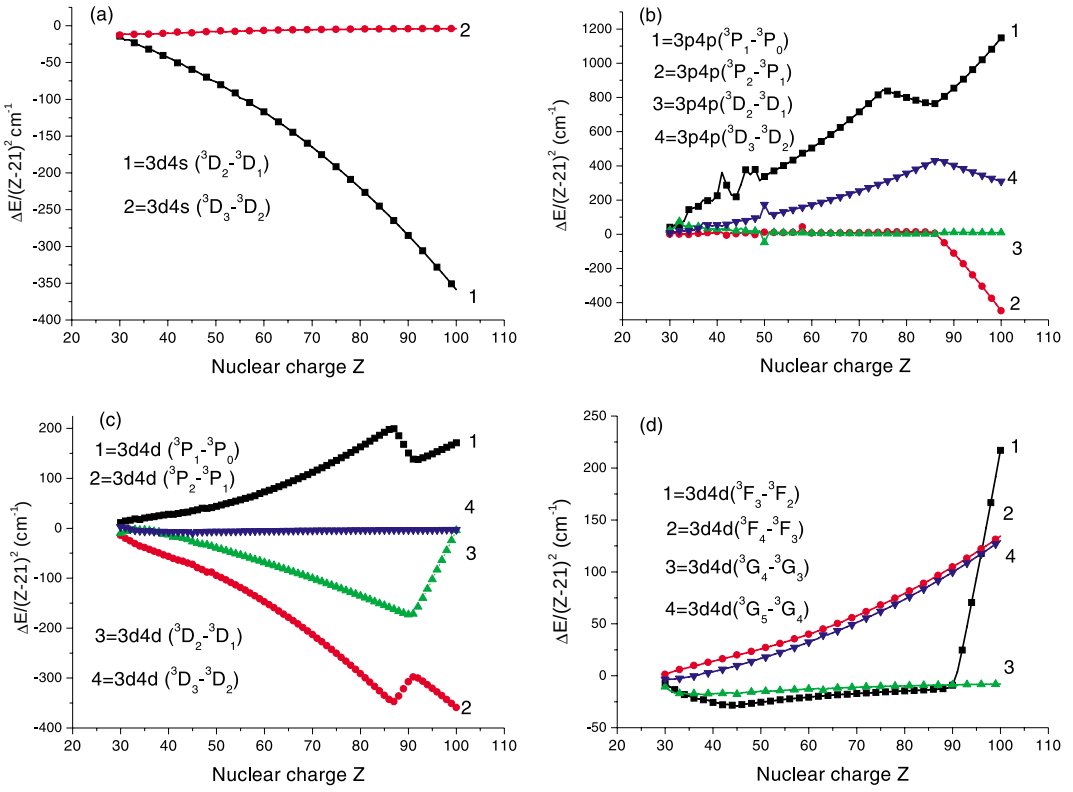

very helpful in verifying the correctness of these sometimes sensitive mixing parameters. We can see the sharp feature in curves shown in Fig. 1 around $Z = 41$–42 and $Z = 75$–76. These singularities are similar to singularities in the energy diagram discussed in refs. 5 and 6. It is mentioned [6] that these sharp features disappear when $3l5l'$ and $3l6l'$ states are included in a model space.

4. Electric-dipole and electric-quadrupole matrix elements

We calculate electric-dipole (E1) matrix elements for the transitions between the 13 odd-parity $3d_j4p_{j'}(1)$, $3d_j4f_{j'}(1)$, $3p_j4s_{1/2}(1)$, $3p_j4d_{j'}(1)$, and $3s_{1/2}4p_{j'}(1)$ excited states and the ground state, and electric-quadrupole (E2) matrix elements between the 14 even-parity $3d_j4s_{1/2}(2)$, $3d_j4d_{j'}(2)$, $3p_j4p_{j'}(2)$, $3p_j4f_{j'}(2)$, and $3s_{1/2}4d_{j'}(2)$ excited states and the ground state for Ni-like ions with nuclear charges $Z = 30$–100. Analytical expressions for multipole matrix elements in the second-order RMBPT are given by (2.12)–(2.17) of ref. 6. First-order electric-dipole and electric-qudrupole matrix elements together with derivative terms are presented in the Appendix.

The first- and second-order Coulomb corrections and second-order Breit–Coulomb corrections to reduced E1 and E2 matrix elements will be referred to as $Z^{(1)}$, $Z^{(2)}$, and $B^{(2)}$, respectively, throughout the text. These contributions are calculated in both length and velocity gauges. In this section, we show the importance of the different contributions and discuss the gauge dependence of the E1 and E2 matrix elements.

Table 5. E1 and E2 uncoupled reduced matrix elements in length L and velocity V forms for transitions from $av(J)$ states with $J = 1$ into the ground state in W^{46+}.

$av(J)$	$Z_L^{(1)}$	$Z_V^{(1)}$	$Z_L^{(2)}$	$Z_V^{(2)}$	$B_L^{(2)}$	$B_V^{(2)}$	$P_L^{(\mathrm{deriv})}$	$P_V^{(\mathrm{deriv})}$
E1 uncoupled reduced matrix elements								
$3d_{3/2}4p_{1/2}(1)$	−0.058467	−0.054955	−0.002220	−0.002167	0.000051	0.000185	−0.058082	0.000151
$3d_{5/2}4p_{3/2}(1)$	−0.064023	−0.060061	−0.003656	−0.003010	0.000035	0.000157	−0.063601	−0.000013
$3d_{3/2}4p_{3/2}(1)$	−0.019017	−0.017913	−0.001320	−0.001060	−0.000028	0.000028	−0.018784	0.000180
$3d_{5/2}4f_{5/2}(1)$	−0.065946	−0.062474	0.002540	0.000584	−0.000138	0.000058	−0.065944	−0.000430
$3d_{5/2}4f_{7/2}(1)$	−0.293391	−0.278016	0.011451	0.002497	−0.000496	0.000220	−0.291188	0.002462
$3d_{3/2}4f_{5/2}(1)$	0.238430	0.226128	−0.009886	−0.002767	0.000558	−0.000186	0.237106	−0.001017
$3p_{3/2}4s_{1/2}(1)$	0.078769	0.074300	0.002654	0.002831	0.000253	−0.000005	0.078222	−0.000046
$3p_{1/2}4s_{1/2}(1)$	−0.037928	−0.035887	−0.003080	−0.002773	−0.000292	−0.000125	−0.037380	0.000346
$3p_{3/2}4d_{3/2}(1)$	−0.049494	−0.046976	0.000266	−0.000310	−0.000152	0.000006	−0.049208	−0.000108
$3p_{3/2}4d_{5/2}(1)$	0.140049	0.133133	−0.000341	0.001179	0.000546	0.000102	0.138327	−0.001408
$3p_{1/2}4d_{3/2}(1)$	−0.082946	−0.078829	−0.000325	−0.000970	−0.000713	−0.000365	−0.081919	0.000538
$3s_{1/2}4p_{1/2}(1)$	−0.054338	−0.051506	−0.003111	−0.003271	−0.000084	0.000038	−0.053715	0.000141
$3s_{1/2}4p_{3/2}(1)$	0.053584	0.050877	0.021778	0.020437	0.000947	0.000774	0.052474	−0.000709
E2 uncoupled reduced matrix elements								
$3d_{5/2}4s_{1/2}(2)$	0.028181	0.026386	0.000341	0.000375	0.000053	0.000009	0.056303	0.026423
$3d_{3/2}4s_{1/2}(2)$	0.021351	0.020057	0.000318	0.000358	0.000064	0.000015	0.042592	0.019965
$3d_{5/2}4d_{3/2}(2)$	−0.017197	−0.016278	−0.000217	−0.000297	−0.000026	−0.000000	−0.034360	−0.016333
$3d_{5/2}4d_{5/2}(2)$	0.033205	0.031479	0.000500	0.000677	0.000066	0.000014	0.066227	0.031364
$3d_{3/2}4d_{3/2}(2)$	0.024533	0.023270	0.000354	0.000485	0.000061	0.000011	0.048929	0.023184
$3d_{3/2}4d_{5/2}(2)$	0.015476	0.014702	0.000273	0.000352	0.000047	0.000013	0.030809	0.014540
$3p_{3/2}4p_{1/2}(2)$	−0.031164	−0.029514	−0.000356	−0.000477	−0.000055	0.000003	−0.062199	−0.029525
$3p_{3/2}4p_{3/2}(2)$	0.026883	0.025535	0.000491	0.000553	0.000073	0.000015	0.053561	0.025406
$3p_{1/2}4p_{3/2}(2)$	−0.020004	−0.019030	0.001058	0.000933	−0.000096	−0.000033	−0.039756	−0.018802
$3p_{3/2}4f_{5/2}(2)$	0.031555	0.030092	0.000261	0.000696	0.000099	0.000018	0.062982	0.030103
$3p_{3/2}4f_{7/2}(2)$	0.077018	0.073465	0.001189	0.002237	0.000215	0.000025	0.153256	0.072565
$3p_{1/2}4f_{5/2}(2)$	0.050777	0.048476	0.012232	0.012550	0.000155	−0.000015	0.101160	0.048194
$3s_{1/2}4d_{3/2}(2)$	0.029103	0.027766	−0.001621	−0.001355	0.000040	−0.000011	0.057942	0.027658
$3s_{1/2}4d_{5/2}(2)$	−0.034254	−0.032712	0.000100	−0.000171	−0.000081	−0.000017	−0.068015	−0.032239

Table 6. E1 and E2 coupled reduced matrix elements in length L and velocity V forms for transitions from $av(J)$ states into the ground state in W^{46+}.

		First order		RMBPT	
$av(J)$	$av(LSJ)$	L	V	L	V
E1 coupled reduced matrix elements					
$3d_{3/2}4p_{1/2}(1)$	$3d4p\,^3P_1$	−0.058310	−0.054843	−0.060387	−0.060268
$3d_{5/2}4p_{3/2}(1)$	$3d4p\,^3D_1$	0.077184	0.072498	0.080784	0.080607
$3d_{3/2}4p_{3/2}(1)$	$3d4p\,^1P_1$	−0.024089	−0.022704	−0.025563	−0.025497
$3d_{5/2}4f_{5/2}(1)$	$3d4f\,^3P_1$	−0.084916	−0.080155	−0.087317	−0.087167
$3d_{5/2}4f_{7/2}(1)$	$3d4f\,^3D_1$	−0.008862	−0.008402	−0.008672	−0.008674
$3d_{3/2}4f_{5/2}(1)$	$3d4f\,^1P_1$	−0.195115	−0.184837	−0.187815	−0.187809
$3p_{3/2}4s_{1/2}(1)$	$3p4s\,^1P_1$	−0.331733	−0.314553	−0.318319	−0.318362
$3p_{1/2}4s_{1/2}(1)$	$3p4s\,^3P_1$	−0.031758	−0.030059	−0.035852	−0.035692
$3p_{3/2}4d_{3/2}(1)$	$3p4d\,^3P_1$	0.033520	0.031780	0.033500	0.033480
$3p_{3/2}4d_{5/2}(1)$	$3p4d\,^1P_1$	0.139072	0.132217	0.139603	0.139504
$3p_{1/2}4d_{3/2}(1)$	$3p4d\,^3D_1$	0.083642	0.079391	0.086667	0.086502
$3s_{1/2}4p_{1/2}(1)$	$3s4p\,^3P_1$	−0.042780	−0.040726	−0.042137	−0.042160
$3s_{1/2}4p_{3/2}(1)$	$3s4p\,^1P_1$	0.043847	0.041632	0.066358	0.065302
E2 coupled reduced matrix elements					
$3d_{5/2}4s_{1/2}(2)$	$3d4s\,^3D_2$	−0.028768	−0.026948	−0.027295	−0.027378
$3d_{3/2}4s_{1/2}(2)$	$3d4s\,^1D_2$	−0.022467	−0.021110	−0.021455	−0.021512
$3d_{5/2}4d_{3/2}(2)$	$3d4d\,^3P_2$	0.015192	0.014377	0.014621	0.014647
$3d_{5/2}4d_{5/2}(2)$	$3d4d\,^3D_2$	0.034461	0.032672	0.033378	0.033425
$3d_{3/2}4d_{3/2}(2)$	$3d4d\,^3F_2$	−0.026663	−0.025291	−0.025869	−0.025904
$3d_{3/2}4d_{5/2}(2)$	$3d4d\,^1D_2$	−0.016388	−0.015569	−0.015898	−0.015920
$3p_{3/2}4p_{1/2}(2)$	$3p4p\,^3D_2$	−0.030345	−0.028747	−0.029200	−0.029253
$3p_{3/2}4p_{3/2}(2)$	$3p4p\,^1D_2$	−0.026678	−0.025350	−0.025907	−0.025945
$3p_{1/2}4p_{3/2}(2)$	$3p4p\,^3P_2$	−0.027505	−0.026190	−0.025353	−0.025499
$3p_{3/2}4f_{5/2}(2)$	$3p4f\,^3D_2$	0.002730	0.002614	0.002928	0.002908
$3p_{3/2}4f_{7/2}(2)$	$3p4f\,^1D_2$	−0.080639	−0.076922	−0.079163	−0.079185
$3p_{1/2}4f_{5/2}(2)$	$3p4f\,^3F_2$	0.054854	0.052369	0.065466	0.065092
$3s_{1/2}4d_{3/2}(2)$	$3s4d\,^3D_2$	−0.020633	−0.019685	−0.016700	−0.016834
$3s_{1/2}4d_{5/2}(2)$	$3s4d\,^1D_2$	−0.032341	−0.030888	−0.030740	−0.030800

4.1. Example: E1 and E2 matrix elements for W^{46+}

In Table 5, we list values of *uncoupled* first- and second-order E1 and E2 matrix elements $Z^{(1)}$, $Z^{(2)}$, and $B^{(2)}$ together with derivative terms $P^{(\mathrm{deriv})}$, for Ni-like tungsten, $Z = 74$. We list values for the thirteen E1 transitions between odd-parity states with $J = 1$ and the ground state and the fourteen E2 transitions between even-parity states with $J = 2$ and the ground state, respectively. Matrix elements in both length (L) and velocity (V) forms are given. We can see that the first-order matrix elements, $Z_L^{(1)}$ and $Z_V^{(1)}$, differ by 5–10%; however, the L–V differences between second-order matrix elements are much larger for some transitions. It can be also seen from Table 5 that for the E1 transitions the derivative term in length form, $P_L^{(\mathrm{deriv})}$, is almost equal to $Z_L^{(1)}$ but the derivative term in velocity form, $P_V^{(\mathrm{deriv})}$, is smaller than $Z_V^{(1)}$ by three to four orders of magnitude. For the E2 transition, the value of $P^{(\mathrm{deriv})}$ in velocity form almost equals $Z^{(1)}$ in velocity form and the $P^{(\mathrm{deriv})}$ in length form is larger by factor of two than $Z^{(1)}$ in length form.

The values of the E1 and E2 *coupled* reduced matrix elements in length and velocity forms are given in Table 6 for the transitions considered in Table 5. Although we use an intermediate-coupling scheme, it is nevertheless convenient to label the physical states using the jj labelling for high Z and

Fig. 4. The first- and second-order Coulomb corrections ($Z^{(1)}$, $Z^{(2)}$), and second-order Breit–Coulomb corrections ($B^{(2)}$) for (*a*) E1 and (*b*) E2 uncoupled matrix elements for transition between excited and ground states calculated in length (L) and velocity (V) forms in Ni-like ions.

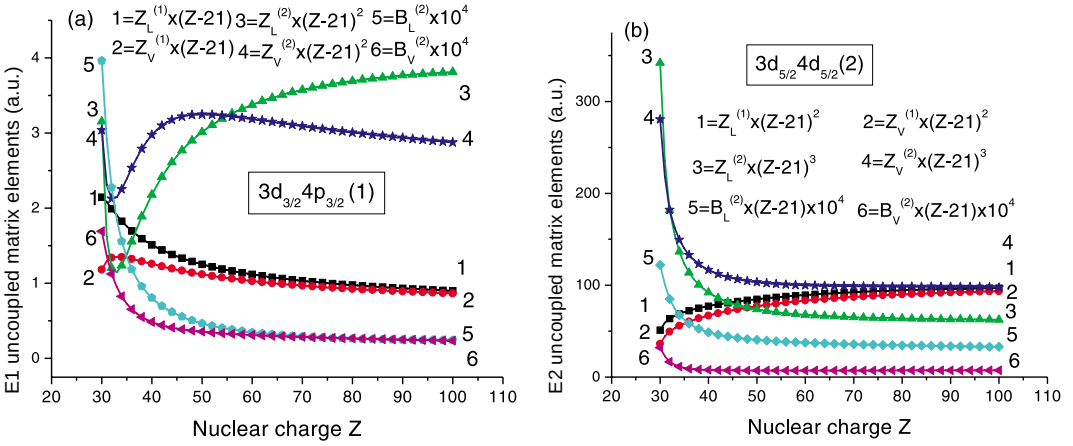

the LS labelling for low Z; both designations are used in Table 6. The first two columns in Table 6 show the L and V values of *coupled* reduced matrix elements calculated in first order. The $L - V$ difference is about 5–10%. Including the second-order contributions (columns headed RMBPT in Table 6) decreases the $L - V$ difference to 0.002–0.2%. This nonzeroth $L - V$ difference arises because we start our RMBPT calculations using a nonlocal Dirac–Fock (DF) potential. If we were to replace the DF potential by a local potential, the differences would disappear completely. It should be emphasized that we include the negative-energy-state (NES) contributions to sum over intermediate states (see ref. 22 for details). Neglecting the NES contributions leads to small changes in the L-form matrix elements but to substantial changes in some of the V-form matrix elements with a consequent loss of gauge independence.

4.2. Z dependencies of E1 and E2 matrix elements in Ni-like ions

In Fig. 4*a*, differences between length and velocity forms are illustrated for the various contributions to uncoupled $0-3d_{3/2}4p_{3/2}(1)$ matrix element, where 0 is the ground state. In the case of E1 transitions, the first-order matrix element $Z^{(1)}$ is proportional to $1/Z$, the second-order Coulomb matrix element $Z^{(2)}$ is proportional to $1/Z^2$, and the second-order Breit–Coulomb matrix element $B^{(2)}$ is almost independent of Z (see ref. 22) for high Z. Therefore, we plot $Z^{(1)} \times (Z-21)$, $Z^{(2)} \times (Z-21)^2$, and $B^{(2)} \times 10^4$ in Fig. 4*a*. As one can see from Fig. 4*a*, all these contributions are positive, except for the second-order Breit–Coulomb matrix elements $B^{(2)}$ in velocity form.

The difference between length and velocity forms for the E2 uncoupled $0 - 3d_{5/2}4d_{5/2}(2)$ matrix element is illustrated in Fig. 4*b*. In the case of E2 transitions, the first-order matrix element $Z^{(1)}$ is proportional to $1/Z^2$, the second-order Coulomb matrix element $Z^{(2)}$ is proportional to $1/Z^3$, and the second-order Breit–Coulomb matrix element $B^{(2)}$ is proportional to $1/Z$ for high Z. Taking into account these dependencies, we plot $Z^{(1)} \times (Z-21)^2$, $Z^{(2)} \times (Z-21)^3$, and $B^{(2)} \times (Z-21) \times 10^4$ in Fig. 4*b*. The second-order Breit–Coulomb correction to the E2 matrix element $B^{(2)}$ is much smaller in velocity form than in length form, as seen in Fig. 4*b*.

The differences between results in length- and velocity-forms shown in Figs. 4*a* and 4*b* are compensated by additional second-order terms called "derivative terms" $P^{(\mathrm{deriv})}$; they are defined by (A.2) (see, also Tables 5 and 6). The derivative terms arise because transition amplitudes depend on the energy, and the transition energy changes order-by-order in RMBPT calculations.

Fig. 5. The first- and second-order corrections ($Z^{(1)}$, $Z^{(2)}$) for (*a*) M1 and (*b*) M2 uncoupled matrix elements for transition between excited and ground states in Ni-like ions. The first-order ($Z^{(1)}$) matrix elements calculated in nonrelativistic ($Z^{(1)}_{\rm NR}$), relativistic frequency-independent($Z^{(1)}_{\rm R}$), and relativistic frequency-dependent ($Z^{(1)}_{\rm RF}$) approximations are presented. The second-order Coulomb ($Z^{(2)}_{\rm CL}$) and Breit–Coulomb corrections ($Z^{(2)}_{\rm BR}$)) are compared.

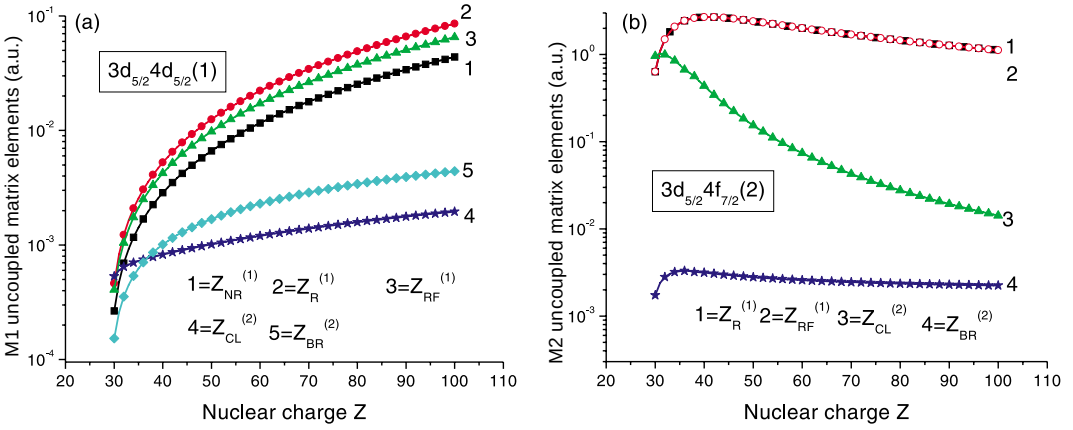

5. Magnetic-dipole and magnetic-quadrupole matrix elements

We calculate magnetic-dipole (M1) matrix elements for the transitions between the 12 even-parity $3d_j4s_{1/2}(1)$, $3d_j4d_{j'}(1)$, $3p_j4p_{j'}(1)$, $3p_j4f_{j'}(1)$, $3s_{1/2}4s_{1/2}(1)$, and $3s_{1/2}4d_{j'}(1)$ excited states and the ground state and magnetic-quadrupole (M2) matrix elements between the 15 odd-parity $3d_j4p_{j'}(2)$, $3d_j4f_{j'}(2)$, $3p_j4s_{1/2}(2)$, $3p_j4d_{j'}(2)$, $3s_{1/2}4p_{j'}(2)$, and $3s_{1/2}4f_{j'}(2)$ excited states and the ground state for Ni-like ions with nuclear charges $Z = 30$–100.

We calculate first- and second-order Coulomb, second-order Breit–Coulomb corrections, and second-order derivative term to reduced M1 and M2 matrix elements $Z^{(1)}$, $Z^{(2)}$, $B^{(2)}$, and $P^{(\rm deriv)}$, respectively, using the method described in eqs. (2.13)–(2.18) of ref. 6 and (A.1), (A.2), (A.8)–(A.14), and (A.23)–(A.25) of the Appendix. In this section, we illustrate the importance of the relativistic and frequency-dependent contributions to the first-order M1 and M2 matrix elements. We also show the importance of the taking into account the second-order RMBPT contributions to M1 and M2 matrix elements and we subsequently discuss the necessity of including the negative-energy contributions to sums over intermediate states.

5.1. *Z* dependencies of M1 and M2 matrix elements in Ni-like ions

The differences between first-order M1 uncoupled matrix elements, calculated in nonrelativistic, relativistic frequency-independent, and relativistic frequency-dependent approximations are illustrated for the $0 - 3d_{5/2}4d_{5/2}(1)$ matrix element in Fig. 5*a*. The corresponding matrix elements are labeled $Z^{(1)}_{\rm RF}$, $Z^{(1)}_{\rm R}$, and $Z^{(1)}_{\rm NR}$. Formulas for relativistic frequency-dependent and nonrelativistic first-order M1 matrix elements are given by (A.8), (A.10), and (A.12) in the Appendix, respectively. We also plot the second-order Coulomb contributions, $Z^{(2)}_{\rm CL}$, and the second-order Breit–Coulomb contributions, $Z^{(2)}_{\rm BR}$, in the same figure. As we observe from Fig. 5a, the values of $Z^{(1)}_{\rm NR}$ are twice as small as the values of $Z^{(1)}_{\rm R}$ and $Z^{(1)}_{\rm RF}$. Therefore, relativistic effects are very large for M1 transitions. The frequency-dependent relativistic matrix elements $Z^{(1)}_{\rm RF}$ differ from the relativistic frequency-independent matrix elements $Z^{(1)}_{\rm R}$ by 10–40%. The differences between other first-order matrix elements calculated with and without frequency dependence are also the order of a few percent. Uncoupled second-order M1 matrix elements $Z^{(2)}_{\rm CL}$ are comparable to first-order matrix elements $Z^{(1)}_{\rm RF}$ for small Z but the relative size of the second-

Fig. 6. The total M1 line strengths ($S_{\rm RF}^{(1+2)}$) between the $3d4d\,^1P_1$ and ground state in Ni-like ions as functions of Z. The first-order ($S^{(1)}$) line strengths calculated in nonrelativistic ($S_{\rm NR}^{(1)}$), relativistic frequency-independent ($S_{\rm R}^{(1)}$), and relativistic frequency-dependent approximations ($S_{\rm RF}^{(1)}$) are presented.

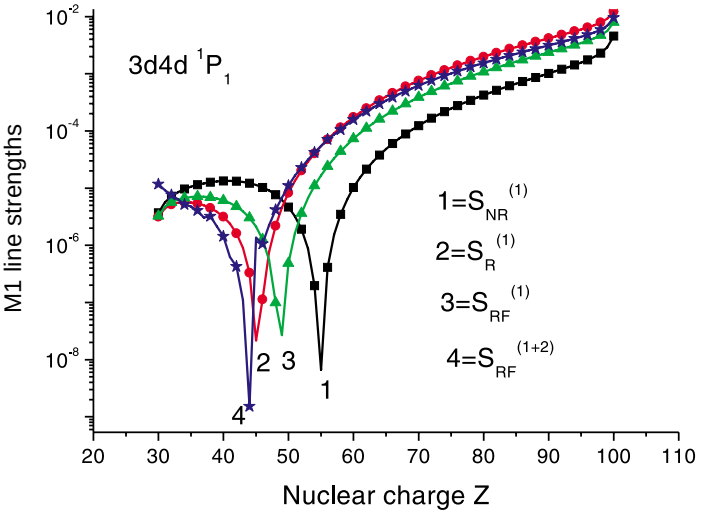

order contribution decreases for high Z. This is expected since second-order Coulomb matrix elements $Z_{\rm CL}^{(2)}$ are proportional to Z for high Z while first-order matrix elements $Z_{\rm RF}^{(1)}$ grow as Z^2. The second-order Breit–Coulomb matrix elements $Z_{\rm BR}^{(2)}$ are proportional to Z^3 and become larger than $Z_{\rm CL}^{(2)}$ for high Z.

The differences between first-order M2 uncoupled matrix elements, calculated in relativistic frequency-dependent and relativistic frequency-independent approximations are illustrated for the $0 - 3d_{5/2}4f_{7/2}(2)$ matrix element in Fig. 5*b*. The corresponding matrix elements are labeled $Z_{\rm RF}^{(1)}$ and $Z_{\rm R}^{(1)}$. Formulas for relativistic frequency-dependent and frequency-independent first-order M2 matrix elements are given by (A.23), and (A.25) in the Appendix, respectively. We also plot the second-order Coulomb contributions, $Z_{\rm CL}^{(2)}$, and the second-order Breit–Coulomb contributions, $Z_{\rm BR}^{(2)}$, in the same figure.

In Fig. 6, we illustrate the Z dependence of the line strengths of M1 transition from the $3d4d\,^1P_1$ excited state to the ground state. In Fig. 6, we plot the values of the first-order line strengths $S_{\rm NR}^{(1)}$, $S_{\rm R}^{(1)}$, and $S_{\rm RF}^{(1)}$ calculated in the same approximations as the M1 uncoupled matrix elements: nonrelativistic, relativistic frequency-independent, and relativistic frequency-dependent approximations, respectively. The total line strengths $S^{(1+2)}$, which include second-order corrections, are also plotted. Strong mixing inside of the even-parity complex with $J = 1$ between $3d_{5/2}4d_{3/2}$ and $3d_{5/2}4d_{5/2}$ states occurring for small Z leads to the sharp features in the line strengths seen in the graphs. The deep minimum in Fig. 6 shifts when different approximations are used for the calculation of line strengths. This shift in the placement of the minimum leads to difficulties in comparison of data for M1 transitions obtained in nonrelativistic and relativistic approximations. We discuss this question further in the next section.

5.2. Example: M1 and M2 matrix elements for W^{46+}

Ab initio relativistic calculations require careful treatment of negative-energy states (NES) (virtual electron–positron pairs). In second-order matrix elements, such contributions arise explicitly from those terms in the sum over states for which $\varepsilon_i < -mc^2$. The effect of the NES contributions to M1 amplitudes has been studied recently in ref. 26. The NES contributions drastically change the second-order Breit–Coulomb matrix elements $B^{(2)}$. However, the second-order Breit–Coulomb correction contributes only

Table 7. M1 uncoupled reduced matrix for transitions from even-parity states with $J = 1$ into the ground state in W^{46+}.

$av(J)$	$Z^{(1)}_{NR}$	$Z^{(1)}_{RN}$	$Z^{(1)}_{RF}$	$Z^{(2)}$	$B^{(2)}_{(pos)}$	$B^{(2)}_{(neg)}$	$P^{(deriv)}$
$3d_{3/2}4s_{1/2}$	0.000000	−0.000174	0.000408	−0.000004	0.000006	0.000095	0.001568
$3d_{5/2}4d_{3/2}$	−0.032954	−0.035971	−0.033363	−0.001009	0.000483	−0.000530	−0.028162
$3d_{5/2}4d_{5/2}$	−0.020691	−0.039891	−0.030614	−0.001467	0.000071	−0.003165	−0.012102
$3d_{3/2}4d_{3/2}$	−0.007499	−0.016060	−0.015197	−0.000584	−0.000006	−0.001331	−0.013466
$3d_{3/2}4d_{5/2}$	−0.024780	−0.021826	−0.024389	−0.000371	0.000404	0.000547	−0.029501
$3p_{3/2}4p_{1/2}$	−0.097709	−0.101061	−0.098271	−0.001655	0.000779	−0.000356	−0.092707
$3p_{3/2}4p_{3/2}$	−0.015809	−0.030442	−0.022188	−0.001136	0.000075	−0.001771	−0.005733
$3p_{1/2}4p_{1/2}$	0.002664	0.006233	0.007228	0.000235	0.000032	0.000414	0.009202
$3p_{1/2}4p_{3/2}$	0.077145	0.074047	0.076584	0.000837	−0.000512	−0.000402	0.081633
$3p_{3/2}4f_{5/2}$	0.000000	−0.007711	−0.003544	−0.000355	0.000008	−0.000797	0.004756
$3s_{1/2}4s_{1/2}$	0.008716	0.016561	0.010950	0.001212	−0.000017	0.000748	−0.000223
$3s_{1/2}4d_{3/2}$	0.000000	−0.003255	−0.000813	0.000298	0.000007	−0.000124	0.004039

2–5% to uncoupled M1 matrix elements and, as a result, negative-energy states change the total values of M1 matrix elements by a few percent only.

In Table 7, we list values of *uncoupled* first- and second-order M1 matrix elements $Z^{(1)}$, $Z^{(2)}$, $B^{(2)}$, together with derivative terms $P^{(deriv)}$, for Ni-like tungsten, $Z = 74$. We list values for the 12 M1 transitions between even-parity states with $J = 1$ and the ground state. The difference between M1 uncoupled matrix elements, calculated in different approximations, is illustrated by the three first columns of Table 7. The importance of NES is illustrated for the second-order Breit–Coulomb matrix elements $B^{(2)}$. In Table 7, we compare the values of $B^{(2)}_{(pos)}$ and $B^{(2)}_{(neg)}$ calculated with positive and negative parts of the spectra, respectively. The value of $B^{(2)}_{(neg)}$ is sometimes even larger than the value of $B^{(2)}_{(pos)}$, and including NES changes the Breit–Coulomb matrix elements by a factor of 10.

In Table 8, we list values of *uncoupled* first- and second-order M2 matrix elements $Z^{(1)}$, $Z^{(2)}$, and $B^{(2)}$, together with derivative terms $P^{(deriv)}$, for Ni-like tungsten, $Z = 74$. We list values for the 15 M2 transitions between odd-parity states with $J = 2$ and the ground state. We note that the first-order M2 matrix elements $0 - 3d_{3/2}4p_{3/2}(2)$, $0 - 3d_{5/2}4f_{5/2}(2)$, and $0 - 3p_{3/2}4d_{3/2}(2)$ vanish because the corresponding factor $(\kappa_a + \kappa_v)$, where κ_i is a relativistic angular momentum quantum number of a state i, in (A.23) for $Z^{(1)}$ equals zero for this transition. Differences between first-order uncoupled M2 matrix elements calculated with and without frequency dependence are shown in first two columns of Table 8 labeled $Z^{(1)}_{R}$ and $Z^{(1)}_{RF}$. As one can see from Table 8, the difference between $Z^{(1)}_{R}$ and $Z^{(1)}_{RF}$ is about 1%. The importance of the NES is illustrated for the second-order Breit–Coulomb matrix elements $B^{(2)}$. In Table 8, we compare the values of $B^{(2)}_{(pos)}$ and $B^{(2)}_{(neg)}$ calculated with positive and negative part of the spectra, respectively. The ratio of $B^{(2)}_{(neg)}$ to $B^{(2)}_{(pos)}$ is about 10%.

5.3. Example: E1, E2, M1, and M2 transition rates for W^{46+}

The E1, E2, M1, and M2 transition probabilities A (s^{-1}) for the transitions between the ground state and $3lj4l'j'(J)$ states are obtained in terms of line strengths S (a.u.) and wavelength λ(Å) as

$$A(E1) = \frac{2.02613 \times 10^{18}}{(2J+1)\lambda^3}\, S(E1), \qquad A(E2) = \frac{1.11995 \times 10^{18}}{(2J+1)\lambda^5}\, S(E2)$$
$$A(M1) = \frac{2.69735 \times 10^{13}}{(2J+1)\lambda^3} S(M1), \qquad A(M2) = \frac{1.49097 \times 10^{13}}{(2J+1)\lambda^5}\, S(M2) \tag{3}$$

Table 8. M2 uncoupled reduced matrix for transitions from odd-parity states with $J = 2$ into the ground state in W^{46+}.

$av(J)$	$Z^{(1)}_{RN}$	$Z^{(1)}_{RF}$	$Z^{(2)}$	$B^{(2)}_{(pos)}$	$B^{(2)}_{(neg)}$	$P^{(deriv)}$
$3d_{5/2}4p_{1/2}$	−0.163836	−0.163043	−0.002595	0.000418	−0.000049	−0.324499
$3d_{5/2}4p_{3/2}$	−0.285213	−0.283560	−0.002356	0.000285	−0.000119	−0.563816
$3d_{3/2}4p_{1/2}$	−0.045303	−0.045467	0.000251	0.000079	−0.000020	−0.091263
$3d_{3/2}4p_{3/2}$	0.000000	0.000000	0.000645	−0.000007	−0.000003	0.000000
$3d_{5/2}4f_{5/2}$	0.000000	0.000000	0.002448	−0.000014	−0.000056	0.000000
$3d_{5/2}4f_{7/2}$	−1.590367	−1.585966	−0.037939	−0.002489	0.000082	−3.163131
$3d_{3/2}4f_{5/2}$	0.448687	0.448339	0.007853	0.001035	−0.000089	0.895981
$3d_{3/2}4f_{7/2}$	0.585334	0.583257	0.019392	0.001235	−0.000089	1.162362
$3p_{3/2}4s_{1/2}$	0.308057	0.306121	0.005528	0.000728	0.000079	0.608371
$3p_{3/2}4d_{3/2}$	0.000000	0.000000	0.001616	−0.000026	−0.000026	0.000000
$3p_{3/2}4d_{5/2}$	0.621628	0.617660	0.009966	0.001636	0.000107	1.227386
$3p_{1/2}4d_{3/2}$	−0.063771	−0.064179	0.002136	−0.000283	−0.000002	−0.129175
$3p_{1/2}4d_{5/2}$	0.196819	0.194852	0.002998	0.000990	0.000025	0.385771
$3s_{1/2}4p_{3/2}$	0.211407	0.208579	−0.027184	−0.001118	0.000087	0.411504
$3s_{1/2}4f_{5/2}$	0.001902	0.000711	0.005294	−0.000184	0.000108	−0.000958

Table 9. E1 and M2 transition rates (A_r in s^{-1}) and wavelengths (λ in Å) for transitions from odd-parity states with $J = 1$ and 2 into the ground state in W^{46+}.

$av(J)$	$av(LS)$	A^{E1}_r	λ^{E1}	$av(J)$	$av(LS)$	A^{M2}_r	λ^{M2}
$3d_{3/2}4p_{1/2}(1)$	$3d4p\,^3D$	6.684[12]	7.174	$3d_{5/2}4p_{1/2}(2)$	$3d4p\,^3F$	4.051[06]	7.477
$3d_{5/2}4p_{3/2}(1)$	$3d4p\,^1P$	1.272[13]	7.027	$3d_{5/2}4p_{3/2}(2)$	$3d4p\,^3P$	1.281[05]	7.188
$3d_{3/2}4p_{3/2}(1)$	$3d4p\,^3P$	1.420[12]	6.778	$3d_{3/2}4p_{1/2}(2)$	$3d4p\,^1D$	1.408[07]	7.032
$3d_{5/2}4f_{5/2}(1)$	$3d4f\,^3P$	2.414[11]	5.953	$3d_{3/2}4p_{3/2}(2)$	$3d4p\,^3D$	4.509[03]	6.768
$3d_{5/2}4f_{7/2}(1)$	$3d4f\,^3D$	1.181[14]	5.870	$3d_{5/2}4f_{5/2}(2)$	$3d4f\,^3P$	3.173[07]	6.164
$3d_{3/2}4f_{5/2}(1)$	$3d4f\,^1P$	3.733[14]	5.689	$3d_{5/2}4f_{7/2}(2)$	$3d4f\,^3D$	1.666[08]	5.938
$3p_{3/2}4s_{1/2}(1)$	$3p4s\,^1P$	2.218[13]	6.154	$3d_{3/2}4f_{5/2}(2)$	$3d4f\,^1D$	8.733[08]	5.923
$3p_{1/2}4s_{1/2}(1)$	$3p4s\,^3P$	5.714[12]	5.345	$3d_{3/2}4f_{7/2}(2)$	$3d4f\,^3F$	7.053[06]	5.753
$3p_{3/2}4d_{3/2}(1)$	$3p4d\,^3P$	5.252[12]	5.255	$3p_{3/2}4s_{1/2}(2)$	$3p4s\,^3P$	2.101[08]	5.744
$3p_{3/2}4d_{5/2}(1)$	$3p4d\,^1P$	9.402[13]	5.201	$3p_{3/2}4d_{3/2}(2)$	$3p4d\,^3F$	1.134[06]	5.247
$3p_{1/2}4d_{3/2}(1)$	$3p4d\,^3D$	5.007[13]	4.679	$3p_{3/2}4d_{5/2}(2)$	$3p4d\,^3P$	2.336[08]	5.203
$3s_{1/2}4p_{1/2}(1)$	$3s4p\,^3P$	1.213[13]	4.635	$3p_{1/2}4d_{3/2}(2)$	$3p4d\,^3D$	4.088[06]	4.648
$3s_{1/2}4p_{3/2}(1)$	$3s4p\,^1P$	3.320[13]	4.492	$3p_{1/2}4d_{5/2}(2)$	$3p4d\,^1D$	4.947[07]	4.612
				$3s_{1/2}4p_{3/2}(2)$	$3s4p\,^3P$	2.292[07]	4.494
				$3s_{1/2}4f_{5/2}(2)$	$3s4f\,^3F$	1.270[05]	4.023

In Tables 9 and 10, we present our RMBPT calculations for E1, M2, E2, and M1 transition rates and wavelengths in the case of Ni-like tungsten, $Z = 74$.

6. Comparison of results with other theory and experiment

We calculate energies of the 50 even-parity $3d_j4s_{1/2}(J)$, $3d_j4d_{j'}(J)$, $3p_j4p_{j'}(J)$, $3p_j4f_{j'}(J)$, $3s_{1/2}4s_{1/2'}(J)$, and $3s_{1/2}4d_{j'}(J)$ excited states and 56 odd-parity $3d_j4p_{j'}(J)$, $3d_j4f_{j'}(J)$, $3p_j4s_{1/2}(J)$, $3p_j4d_{j'}(J)$, $3s_{1/2}4p_{j'}(J)$, and $3s_{1/2}4f_{j'}(J)$ excited states for Ni-like ions with nuclear charges ranging from $Z = 30$–100. Reduced matrix elements, oscillator strengths, and transition rates are determined for

Table 10. E2 and M1 transition rates (A_r in s^{-1}) and wavelengths (λ in Å) for transitions from even-parity states with $J = 2$ and 1 into the ground state in W^{46+}.

$av(J)$	$av(LS)$	A_r^{E2}	λ^{E2}	$av(J)$	$av(LS)$	A_r^{M1}	λ^{M1}
$3d_{5/2}4s_{1/2}(2)$	$3d4s\,^3D$	5.320[09]	7.929	$3d_{3/2}4s_{1/2}(1)$	$3d4s\,^3D$	1.633[04]	7.614
$3d_{3/2}4s_{1/2}(2)$	$3d4s\,^1D$	4.042[09]	7.608	$3d_{5/2}4d_{3/2}(1)$	$3d4d\,^3S$	6.929[07]	6.508
$3d_{5/2}4d_{3/2}(2)$	$3d4d\,^3P$	4.181[09]	6.487	$3d_{5/2}4d_{5/2}(1)$	$3d4d\,^1P$	3.141[07]	6.428
$3d_{5/2}4d_{5/2}(2)$	$3d4d\,^3D$	2.321[10]	6.405	$3d_{3/2}4d_{3/2}(1)$	$3d4d\,^3D$	1.427[07]	6.276
$3d_{3/2}4d_{3/2}(2)$	$3d4d\,^3F$	1.568[10]	6.258	$3d_{3/2}4d_{5/2}(1)$	$3d4d\,^3P$	2.150[07]	6.212
$3d_{3/2}4d_{5/2}(2)$	$3d4d\,^1D$	6.210[09]	6.198	$3p_{3/2}4p_{1/2}(1)$	$3p4p\,^3D$	4.271[08]	5.881
$3p_{3/2}4p_{1/2}(2)$	$3p4p\,^3D$	2.749[10]	5.878	$3p_{3/2}4p_{3/2}(1)$	$3p4p\,^3S$	1.908[07]	5.607
$3p_{3/2}4p_{3/2}(2)$	$3p4p\,^1D$	2.768[10]	5.595	$3p_{1/2}4p_{1/2}(1)$	$3p4p\,^1P$	3.682[06]	5.134
$3p_{1/2}4p_{3/2}(2)$	$3p4p\,^3P$	5.045[10]	4.921	$3p_{1/2}4p_{3/2}(1)$	$3p4p\,^3P$	3.975[08]	4.928
$3p_{3/2}4f_{5/2}(2)$	$3p4f\,^3D$	6.945[08]	4.888	$3p_{3/2}4f_{5/2}(1)$	$3p4f\,^3D$	2.022[05]	4.898
$3p_{3/2}4f_{7/2}(2)$	$3p4f\,^1D$	5.234[11]	4.858	$3s_{1/2}4s_{1/2}(1)$	$3s4s\,^3S$	6.645[07]	4.842
$3p_{1/2}4f_{5/2}(2)$	$3p4f\,^3F$	6.220[11]	4.354	$3s_{1/2}4d_{3/2}(1)$	$3s4d\,^3D$	3.173[04]	4.267
$3s_{1/2}4d_{3/2}(2)$	$3s4d\,^3D$	4.507[10]	4.265				
$3s_{1/2}4d_{5/2}(2)$	$3s4d\,^1D$	1.586[11]	4.233				

E1, M1, E2, and M2 allowed and forbidden transitions into the ground state for each ions. Comparisons are also given with other theoretical results and with experimental data. Our results are presented in two parts: E1, M1, E2, and M2 wavelengths and transition probabilities.

6.1. Transition wavelengths

In Table 11, we compare our RMBPT results for wavelengths with theoretical results presented by Biémont in ref. 17 and experimental results given in ref. 16.

In particular, we list results for transitions between $3d4s$, $3d4p$ excited states and the ground state for ions ($Z = 92$, 90, 83, 80, 70, 60, and 50) presented by Biémont in ref. 17. We did not repeat comparison with experimental data given in our previous paper [6]. It should be noted that we improved our results [6] including nondiagonal energy-matrix elements. A new computer code was developed that allows us to consider not only the high-Z ions ($Z \geq 47$) as was done previously [6] but also the low-Z ions ($30 \leq Z \leq 46$). It is well-known that there is almost no deviation from the pure jj coupling scheme for high-Z Ni-like ions and we found only very small difference (0.003–0.01% for $Z = 50$) in wavelengths between our present results and results given in ref. 6. The difference between our present RMBPT results and MCDF results given by Biémont in ref. 17 is much larger (0.5–1% for $Z = 50$). As can be seen from Table 11, our results are in better agreement with experiment [16] than the MCDF results from ref. 17.

Our results are in excellent agreement with experimental results for the energy of the E2 and M3 transitions presented by Beiersdorfer et al. in ref. 18.

For Z = 90

	RMBPT	Expt.
$E(3d_{5/2}4s_{1/2}(2)) =$	2560.7 eV,	2561.3 ± 0.2 eV
$E(3d_{5/2}4s_{1/2}(3)) =$	2558.2 eV,	2558.7 ± 0.2 eV

For Z = 92

$E(3d_{5/2}4s_{1/2}(2)) =$	2692.4 eV,	2691.9 ± 0.2 eV
$E(3d_{5/2}4s_{1/2}(3)) =$	2689. 8eV,	2689.3 ± 0.2 eV (4)

Table 11. Wavelengths (λ in Å) for transitions from $3dj4lj'(J)$ states to the ground state in Ni-like ions. Comparison of (a) our RMBPT results with (b) theoretical results presented by Biémont in ref. 17 and (c) experimental results given in ref. 16.

		Z						
		92	90	83	80	70	60	50
$3d_{3/2}4s_{1/2}$ (1)	(a)	4.306	4.543	5.579	6.149	8.927	14.349	27.344
	(b)	4.318	4.556	5.593	6.163	8.951	14.403	27.518
$3d_{3/2}4s_{1/2}$ (2)	(a)	4.304	4.541	5.576	6.145	8.920	14.334	27.299
	(b)	4.316	4.553	5.589	6.159	8.944	14.388	27.473
$3d_{5/2}4s_{1/2}$ (2)	(a)	4.605	4.842	5.880	6.453	9.254	14.725	27.793
	(b)	4.617	4.854	5.810	6.467	9.277	14.777	28.007
$3d_{5/2}4s_{1/2}$ (3)	(a)	4.609	4.847	5.886	6.460	9.265	14.747	27.885
	(b)	4.621	4.859	5.899	6.474	9.289	14.801	28.066
$3d_{3/2}4p_{3/2}$ (0)	(a)	3.704	3.930	4.907	5.438	7.998	12.910	24.373
	(b)	3.710	3.936	4.914	5.447	8.017	12.951	24.512
$3d_{3/2}4p_{1/2}$ (1)	(a)	4.095	4.318	5.287	5.817	8.383	13.312	24.817
	(b)	4.101	4.324	5.295	5.826	8.401	13.352	24.952
	(c)				5.816	8.377		24.783
$3d_{5/2}4p_{3/2}$ (1)	(a)	3.917	4.145	5.128	5.663	8.239	13.166	24.628
	(b)	3.920	4.149	5.134	5.670	8.254	13.204	24.755
	(c)				5.657	8.235		24.596
$3d_{3/2}4p_{3/2}$ (1)	(a)	3.699	3.924	4.897	5.427	7.978	12.863	24.236
	(b)	3.703	3.929	4.905	5.436	7.996	12.904	24.374
	(c)				5.417	7.978		24.211
$3d_{5/2}4p_{1/2}$ (2)	(a)	4.375	4.598	5.572	6.106	8.700	13.689	25.340
	(b)	4.380	4.607	5.578	6.114	8.715	13.727	25.472
$3d_{5/2}4p_{3/2}$ (2)	(a)	4.101	4.325	5.296	5.827	8.400	13.341	24.871
	(b)	4.108	4.331	5.304	5.837	8.418	13.385	25.014
$3d_{3/2}4p_{1/2}$ (2)	(a)	3.919	4.147	5.131	5.666	8.244	13.175	24.650
	(b)	3.923	4.151	5.137	5.674	8.260	13.215	24.787
$3d_{3/2}4p_{3/2}$ (2)	(a)	3.695	3.920	4.891	5.419	7.965	12.838	24.181
	(b)	3.699	3.925	4.899	5.429	7.994	12.880	24.319
$3d_{5/2}4p_{1/2}$ (3)	(a)	4.373	4.596	5.568	6.102	8.692	13.673	25.288
	(b)	4.378	4.602	5.576	6.111	8.710	13.715	25.430
$3d_{5/2}4p_{3/2}$ (3)	(a)	3.913	4.141	5.123	5.657	8.229	13.148	24.591
	(b)	3.918	4.146	5.130	5.666	8.246	13.189	24.730
$3d_{3/2}4p_{3/2}$ (3)	(a)	3.698	3.923	4.896	5.426	7.978	12.863	24.249
	(b)	3.703	3.929	4.905	5.436	7.996	12.906	24.391
$3d_{5/2}4p_{3/2}$ (4)	(a)	3.922	4.150	5.135	5.672	8.254	13.199	24.718
	(b)	3.926	4.155	5.143	5.680	8.272	13.240	24.863

6.2. The E1, E2, M1, and M2 transition probabilities

We present the resulting transition probabilities (A_r) in Figs. 7–10. Transition rates and oscillator strengths for the seven E1 lines from $3d4p\,^3P_1$, $^3D_1$, $^1P_1$, $3d4f\,^3P_1$, $^3D_1$, $^1P_1$ and $3p4s\,^1P_1$ levels to the ground state are plotted in Fig. 7. The sharp features in the curves shown in these figures can be explained in many cases by a strong mixing of states inside of the odd-parity complex with $J = 1$. The

Fig. 7. E1 transition rates and oscillator strengths between odd-parity states and ground state in Ni-like ions as function of Z.

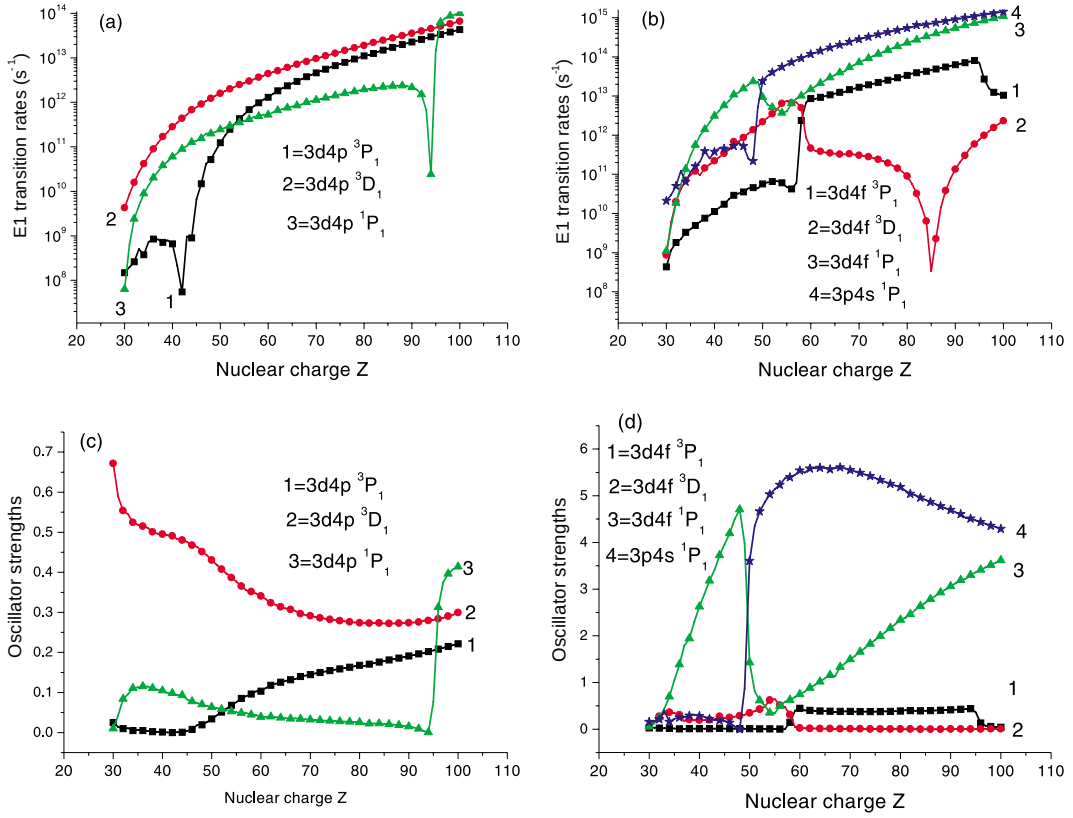

deep minimum in the curve with the $3d4p\,^3P$ label in the $Z = 43$–44 range can be explained by mixing of the $3d_{3/2}4p_{1/2}$ (1) and $3d_{5/2}4p_{3/2}$ (1) states. In Fig. 7*b*, the double cusp in the interval $Z = 57$–59 is due to the mixing of the $3d_{5/2}4f_{5/2}$ (1) and $3d_{5/2}4f_{7/2}$ (1) states. The mixing of the $3d_{5/2}4f_{7/2}$ (1) and $3d_{3/2}4f_{5/2}$ (1) states in the $Z = 55$–56 range gives a singularity in the curve with the $3d4f\,^3D_1$ label. The mixing of the $3d_{3/2}4f_{5/2}$ (1) and $3p_{3/2}4s_{1/2}$ (1) states in the $Z = 49$–50 range gives a singularity in the curves with the $3d4f\,^1P_1$ and $3p4s\,^1P_1$ labels. Most of remaining singularities in the Figs. 7–10 can be explained in a similar way.

Transition rates for the six E2 lines from the $3d4s\,^3D_2$, $^1D_2$ and $3d4d\,^3P_2$, $^3D_2$, $^3F_2$, $^1D_2$ levels to the ground state are plotted in Fig. 8. The curves describing the $3d4s\,^3D_2$, $^1D_2$ transition rates increase smoothly with Z without any sharp features. It should be noted that the difference in values of A_r for the $3d4s\,^3D_2$ and $3d4s\,^1D_2$ lines is about 20%. There is a small difference in the values of A_r for the $3d4d\,^3D_2$, $3d4d\,^3F_2$, and $3d4d\,^1D_2$ lines shown in Fig. 8*b*.

Transition rates for the six M1 lines from the $3d4d\,^3S_1$, $^1P_1$, $^3D_1$, $^3P_1$, $3d4s\,^3D_1$, and $3s4s\,^3S_1$ levels to the ground state are plotted in Fig. 9. The deep minima in Fig. 9*a* for small Z has the same nature as those of the $3d4d\,^1P_1$ line strengths shown on Fig. 6: strong mixing between $3d_{5/2}4d_{3/2}$ and $3d_{5/2}4d_{5/2}$ states. As can be seen from Fig. 9*b*, the value of A_r for the $3s4s\,^3S_1$ line is smaller than the value of A_r for the $3d4s\,^3D_1$ line by a factor of 10^3–10^4.

Transition rates for eight M2 lines from the $3d4p\,^3F_2$, $^3P_2$, $^1D_2$, $^3D_2$ and $3d4f\,^3P_2$, $^3D_2$, $^1D_2$, $^3F_2$ levels to the ground state are plotted in Fig. 10. The sharp features in the curves shown in these figures

Fig. 8. E2 transition rates between even-parity states and ground state in Ni-like ions as function of Z.

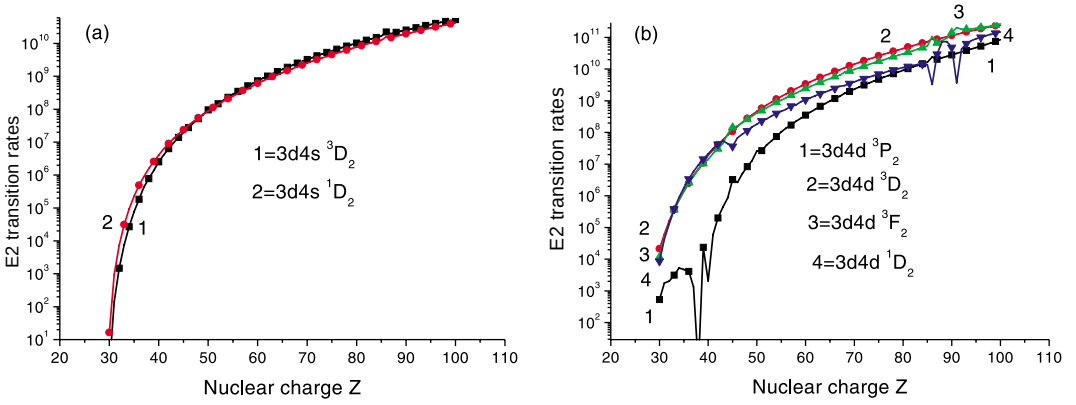

Fig. 9. M1 transition rates between even-parity states and the ground state in Ni-like ions as function of Z.

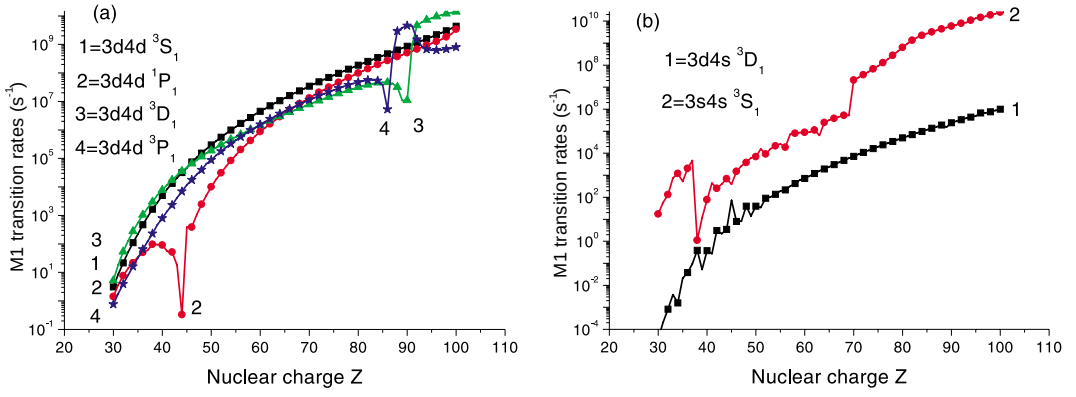

Fig. 10. M2 transition rates between odd-parity states and the ground state in Ni-like ions as function of Z.

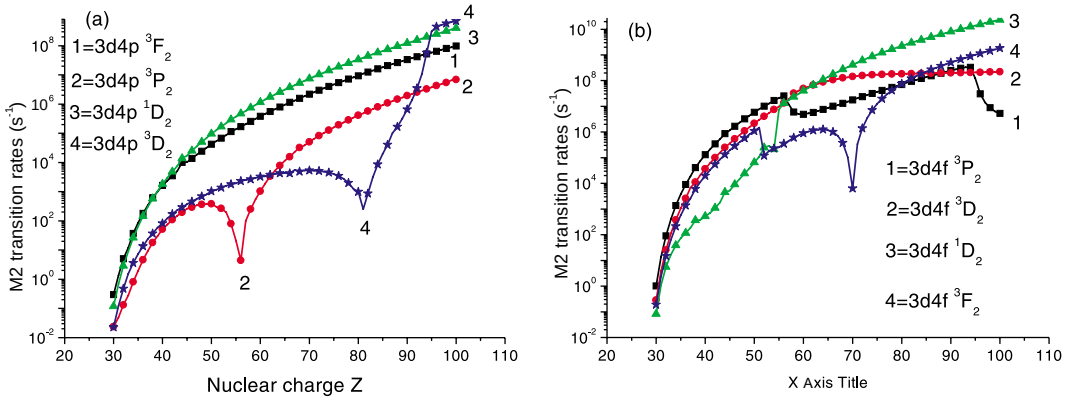

can be explained in many cases as a strong mixing of states inside of the odd-parity $3d_j4p_{j'}$ (2) and $3d_j4f_{j'}$ (2) complexes.

In Table 12, we compare our RMBPT results for E1, E2, M1, and M2 transition rates with the theoretical results presented by Biémont in ref. 17 and Quinet and Biémont in ref. 16. In particular, we list results for transitions between $3d4s$, $3d4p$ excited states and the ground state for ions ($Z = 92$, 90,

Table 12. E1, E2, M1, and M2 transition rates (A_r in s^{-1}) in Ni-like ions for transitions between excited $3dj4lj'(J)$ states and the ground state. Comparison of our (a) RMBPT results with (b) theoretical results presented by Biémont in ref. 17 and (c) results by Quinet in ref. 16.

		Z						
		92	90	83	80	70	60	50
Magnetic-quadrupole transitions								
$3d_{5/2}4p_{1/2}$ (2)	(a)	4.20[7]	3.34[7]	1.42[7]	9.36[6]	2.19[6]	3.81[5]	4.21[4]
	(b)	4.43[7]	3.53[7]	1.51[7]	1.02[7]	2.42[6]	4.41[5]	
$3d_{5/2}4p_{3/2}$ (2)	(a)	2.54[6]	1.94[6]	6.75[5]	4.16[5]	5.05[4]	1.04[3]	3.79[2]
	(b)	3.53[6]	2.71[6]	9.80[5]	6.02[5]			
$3d_{3/2}4p_{1/2}$ (2)	(a)	1.56[8]	1.23[8]	5.07[7]	3.34[7]	7.45[6]	1.16[6]	9.53[4]
	(b)	1.64[8]	1.31[8]	5.63[7]	3.82[7]	8.92[6]	1.48[6]	1.31[5]
$3d_{3/2}4p_{3/2}$ (2)	(a)	3.48[6]	6.51[5]	3.19[3]	9.82[2]	5.32[3]	3.28[3]	1.03[3]
	(b)	1.02[5]						
$3d_{5/2}4f_{5/2}$ (2)	(a)	3.06[8]	2.47[8]	1.06[8]	7.00[7]	1.78[7]	4.93[6]	5.90[6]
$3d_{5/2}4f_{7/2}$ (2)	(a)	2.03[8]	2.00[8]	1.88[8]	1.83[8]	1.43[8]	4.90[7]	2.16[6]
$3d_{3/2}4f_{5/2}$ (2)	(a)	1.01[10]	8.02[9]	3.37[9]	2.23[9]	4.16[8]	4.00[7]	6.48[4]
$3d_{3/2}4f_{7/2}$ (2)	(a)	6.77[8]	5.09[8]	1.51[8]	7.55[7]	6.39[3]	8.94[5]	1.10[6]
Electric-quadrupole transitions								
$3d_{3/2}4s_{1/2}$ (2)	(a)	3.01[10]	2.56[10]	1.38[10]	1.03[10]	3.25[9]	7.29[8]	9.52[7]
	(b)	3.35[10]	2.86[10]	1.33[10]	1.16[10]	3.77[9]	8.86[8]	1.16[8]
$3d_{5/2}4s_{1/2}$ (2)	(a)	2.30[10]	1.95[10]	1.04[10]	7.74[9]	2.51[9]	6.11[8]	8.79[7]
	(b)	2.63[10]	2.24[10]	1.20[10]	8.98[9]	2.98[9]	7.50[8]	1.19[8]
$3d_{5/2}4d_{3/2}$ (2)	(a)	3.48[10]	2.82[10]	1.30[10]	9.15[9]	2.32[9]	3.54[8]	2.59[7]
	(c)				1.01[10]	2.57[9]	3.97[8]	2.03[7]
$3d_{5/2}4d_{5/2}$ (2)	(a)	1.36[11]	1.15[11]	6.03[10]	4.47[10]	1.43[10]	3.38[9]	4.67[8]
	(c)				4.94[10]	1.61[10]	3.89[9]	5.45[8]
$3d_{3/2}4d_{3/2}$ (2)	(a)	1.82[11]	1.40[11]	4.22[10]	3.05[10]	9.78[9]	2.43[9]	4.09[8]
	(c)				3.38[10]	1.10[10]	2.83[9]	4.84[8]
$3d_{3/2}4d_{5/2}$ (2)	(a)	4.27[10]	4.84[10]	1.39[10]	1.12[10]	3.97[9]	1.08[9]	1.80[8]
	(c)				1.25[10]	4.53[9]	1.25[9]	2.35[8]
Magnetic-dipole transitions								
$3d_{3/2}4s_{1/2}$ (1)	(a)	3.32[5]	2.41[5]	8.28[4]	4.95[4]	7.28[3]	7.20[2]	3.91[1]
$3d_{5/2}4d_{3/2}$ (1)	(a)	1.16[9]	8.60[8]	2.97[8]	1.86[8]	3.42[7]	4.48[6]	2.99[5]
$3d_{5/2}4d_{5/2}$ (1)	(a)	6.84[8]	5.05[8]	1.65[8]	9.86[7]	1.32[7]	8.64[5]	1.01[4]
$3d_{3/2}4d_{3/2}$ (1)	(a)	4.59[9]	1.10[7]	4.19[7]	3.12[7]	7.87[6]	1.47[6]	1.89[5]
$3d_{3/2}4d_{5/2}$ (1)	(a)	1.50[9]	4.57[9]	5.72[7]	4.76[7]	1.13[7]	1.55[6]	8.83[4]
Electric-dipole transitions								
$3d_{3/2}4p_{1/2}$ (1)	(a)	2.61[13]	2.28[13]	1.3713]	1.10[13]	4.59[12]	1.31[12]	1.24[11]
	(b)	2.73[13]	2.41[13]	1.4713]	1.17[13]	4.89[12]	1.48[12]	1.48[11]
$3d_{5/2}4p_{3/2}$ (1)	(a)	4.00[13]	3.55[13]	2.3213]	1.90[13]	9.57[12]	4.44[12]	1.59[12]
	(b)	3.66[13]	3.29[13]	2.2313]	1.86[13]	9.62[12]	4.46[12]	1.68[12]
$3d_{3/2}4p_{3/2}$ (1)	(a)	1.50[12]	2.15[12]	2.10[12]	1.94[12]	1.12[12]	5.23[11]	2.43[11]
	(b)	4.38[12]	3.94[12]	2.70[12]	2.27[12]	1.23[12]	6.16[11]	2.01[11]

83, 80, 70, 60, and 50) presented by Biémont in ref. 17. As can be seen from Table 12, the difference between both results is about 5–20% that can be explained by the second-order contribution included in our RMBPT calculations since the results in refs. 16, 17 were obtained using the MCDF approximation.

7. Conclusion

We have presented a systematic second-order relativistic RMBPT study of excitation energies, reduced matrix elements, line strengths, and transition rates for $\Delta n = 1$ electric- and magnetic-dipole and electric- and magnetic-quadrupole transitions in Ni-like ions with nuclear charges $Z = 30$–100. Our calculation of the retarded E1, E2, M1, and M2 matrix elements include correlation corrections from both Coulomb and Breit interactions. Contributions from virtual electron–positron pairs were also included in the second-order matrix elements. Both length and velocity forms of the E1 and E2 matrix elements were evaluated and small differences, caused by the nonlocality of the starting DF potential, were found between the two forms. Second-order RMBPT transition energies were used to evaluate oscillator strengths and transition rates. Good agreement of our RMBPT data with other accurate theoretical results leads us to conclude that the RMBPT method provides accurate data for Ni-like ions. Results from the present calculations provide benchmark values for future theoretical and experimental studies of the nickel isoelectronic sequence.

Acknowledgments

This work was supported by DOE-NNSA/NV Cooperative Agreement DE-FC08-01NV14050 and Sandia National Laboratories.

References

1. E. Avgoustoglou, W.R. Johnson, D.R. Plante, J. Sapirstein, S. Sheinerman, and S.A. Blundell. Phys. Rev. A, **46**, 5478 (1992).
2. E. Avgoustoglou, W.R. Johnson, and J. Sapirstein. Phys. Rev. A, **51**, 1196 (1995).
3. E. Avgoustoglou and Z.W. Liu. Phys. Rev. A, **54**, 1351 (1996).
4. E.N. Avgoustoglou and D.R. Beck. Phys. Rev. A, **57**, 4286 (1998).
5. U.I. Safronova, C. Namba, I. Murakami, W.R. Johnson, and M.S. Safronova. Phys. Rev. A, **64**, 012507 (2001).
6. U.I. Safronova, W.R. Johnson, and J.R. Albritton. Phys. Rev. A, **62**, 052505 (2000).
7. J.H. Scofield and B.J. MacGowan. Phys. Scr. **46**, 361 (1992).
8. M.H. Chen and A.L. Osterheld. Phys. Rev. A, **52**, 3790 (1995).
9. Y. Li, J. Nilsen, J. Dunn, A.L. Osterheld, A. Ryabtsev, and S. Churilov. Phys. Rev. A, **58**, R2668 (1998).
10. H. Daido, S. Ninomiya, M. Takagi, Y. Kato, and F. Koike. J. Opt. Soc. Am. B, **16**, 296 (1999).
11. J. Nilsen, J. Dunn, A.L. Osterheld, and Y. Li. Phys. Rev. A, **60**, R2677 (1999).
12. R. Doron, M. Fraenkel, P. Mandelbaum, A. Zigler, and J.J. Schwob. Phys. Scr. **58**, 19 (1998).
13. A. Zigler, P. Mandelbaum, J.J. Schwob, and D. Mitnik. Phys. Scr. **50**, 61 (1994).
14. M. Busquet, D. Pain, J. Bauche, and E. Luc-Koenig. Phys. Scr. **31**, 137 (1985).
15. M. Klapisch, J.J. Schwob, M. Fraenkel, and J. Oreg. J. Opt. Soc. Am. **61**, 148 (1977).
16. P. Quinet and E. Biémont. Phys. Scr. **43**, 150 (1991) and references therein.
17. E. Biémont. J. Phys. B, **30**, 4207 (1997).
18. P. Beiersdorfer, A.L. Osterheld, J. Scolfield, B. Wargelin, and R.E. Marrs. Phys. Rev. Lett. **67**, 2272 (1991).
19. S.S. Churilov, A.N. Ryabtsev, and J.-F. Wyart. Phys. Scr. **38**, 326 (1988).
20. J.-F. Wyart. Phys. Scr. **36**, 234 (1987).
21. M.S. Safronova, W.R. Johnson, and U.I. Safronova. Phys. Rev. A, **53**, 4036 (1996).
22. U.I. Safronova, W.R. Johnson, M.S. Safronova, and A. Derevianko. Phys. Scr. **59**, 286 (1999).
23. M.H. Chen, K.T. Cheng, and W.R. Johnson. Phys. Rev. A, **47**, 3692 (1993).
24. Y.K. Kim, D.H. Baik, P. Indelicato, and J.P. Desclaux. Phys. Rev. A, **44**, 148 (1991).
25. S.A. Blundell. Phys. Rev. A, **47**, 1790 (1993).
26. U.I. Safronova, W.R. Johnson, and A. Derevianko. Phys. Scr. **60**, 46 (1999).
27. W.R. Johnson, D.R. Plante, and J. Sapirstein. Adv. Atom. Mol. Opt. Phys. **35**, 255 (1995).

Appendix A. Matrix elements

A1. Multipole matrix elements

The first-order reduced multipole matrix element $Z_K^{(1)}$ for a transition between the ground state $|0\rangle$ and the uncoupled particle–hole state $\Phi_{JM}(av)$ of (1) is

$$Z_K^{(1)}[0-av(J)] = \frac{1}{\sqrt{2J+1}} Z_J(av)\delta_{JK} \tag{A.1}$$

The multipole matrix $Z_K(av)$ element, which includes retardation is given below for electric-dipole ($K=1$) and electric-quadrupole ($K=2$) transitions in length and velocity forms and magnetic-dipole ($K=1$) and magnetic-quadrupole ($K=2$) transitions.

The second-order reduced matrix element $Z_K^{(2)}[0-av(J)]$ consists of three contributions: $Z_K^{(\mathrm{RPA})}$, $Z_K^{(\mathrm{HF})}$, and $P_K^{(\mathrm{deriv})}$. The quantity $Z_K^{(\mathrm{RPA})}$, $Z_K^{(\mathrm{HF})}$ are defined by eqs. (2.14), (2.15) of ref. 6. The quantity $P_K^{(\mathrm{deriv})}$ is defined by

$$P_K^{(\mathrm{deriv})}[0-(av)J] = \frac{1}{\sqrt{2J+1}} Z_J^{(\mathrm{deriv})}(av)\delta_{JK} \tag{A.2}$$

The derivative term $Z_K^{(\mathrm{deriv})}(av)$, which includes retardation is given below for E1 and E2 ($K=1$ and $K=2$) transitions in length and velocity forms and M1 and M2 ($K=1$ and $K=2$) transitions.

A2. Electric-dipole matrix elements

The electric-dipole matrix element $Z_1(av)$, which includes retardation, is given in length and velocity forms as

length form

$$Z_1(av) = \langle \kappa_a \| C_1 \| \kappa_v \rangle \frac{3}{k} \int_0^\infty \mathrm{d}r \{ j_1(kr)[G_a(r)G_v(r) + F_a(r)F_v(r)] + j_2(kr)\left[\frac{\kappa_a - \kappa_v}{2}[G_a(r)F_v(r) + F_a(r)G_v(r)] + [G_a(r)F_v(r) - F_a(r)G_v(r)]\right]\Big\} \tag{A.3}$$

velocity form

$$Z_1(av) = \langle \kappa_a \| C_1 \| \kappa_v \rangle \frac{1}{k} \int_0^\infty \mathrm{d}r \{ [j_2(kr) + j_0(kr)][G_a(r)F_v(r) - F_a(r)G_v(r)] - \frac{\kappa_a - \kappa_v}{2}[-j_2(kr) + 2j_0(kr)][G_a(r)F_v(r) + F_a(r)G_v(r)]\Big\} \tag{A.4}$$

The electric-dipole derivative matrix element $Z_1^{\mathrm{deriv}}(av)$, which includes retardation, is given in length and velocity forms as

length form

$$Z_1^{(\mathrm{deriv})}(av) = \langle \kappa_a \| C_1 \| \kappa_v \rangle \frac{3}{k} \int_0^\infty \mathrm{d}r [j_1(kr) - (kr)j_2(kr)][G_a(r)G_v(r) + F_a(r)F_v(r)] + \langle \kappa_a \| C_2 \| \kappa_v \rangle \frac{3}{k} \int_0^\infty \mathrm{d}r [(kr)j_1(kr) - 3j_2(kr)] \times \left[\frac{\kappa_a - \kappa_v}{2}[G_a(r)F_v(r) + F_a(r)G_v(r)] + [G_a(r)F_v(r) - F_a(r)G_v(r)]\right] \tag{A.5}$$

velocity form

$$Z_1^{(\mathrm{deriv})}(av) = \langle \kappa_a \,\|C_1\|\, \kappa_v\rangle \frac{3}{k}\int_0^\infty \mathrm{d}r\,\{[-j_2(kr)]\,[G_a(r)F_v(r) - F_a(r)G_v(r)] - \frac{\kappa_a - \kappa_v}{2}\,[-(kr)\,j_1(kr) + j_2(kr)]\,[G_a(r)F_v(r) + F_a(r)G_v(r)]\Big\} \quad \text{(A.6)}$$

Here κ_a is the angular momentum quantum number [$\kappa_a = \mp(j_a + \frac{1}{2})$ for $j_a = (l_a \pm \frac{1}{2})$], and $k = \omega\alpha$, where $\omega = \varepsilon_v - \varepsilon_a$ is the photon energy and α is the fine-structure constant. The functions $G_a(r)$ and $F_a(r)$ are large- and small-component radial Dirac–Fock wave functions, respectively. The quantity $C_{1q}(\hat{r})$ is a normalized spherical harmonic and $\langle \kappa_a \,\|C_k\|\, \kappa_v\rangle$ is equal to

$$\langle \kappa_a \,\|C_k\|\, \kappa_v\rangle = (-1)^{j_a+1/2}\sqrt{[j_a][j_v]}\begin{pmatrix} j_a & j_v & k \\ -\frac{1}{2} & \frac{1}{2} & 0\end{pmatrix}\pi(l_a + l_v + k) \quad \text{(A.7)}$$

$$= (-1)^{k-j_v-1/2}\sqrt{[j_a][j_v][l_a][l_v]}\begin{pmatrix} l_a & l_v & k \\ 0 & 0 & 0\end{pmatrix}\begin{Bmatrix} j_a & j_v & k \\ l_v & l_a & 1/2\end{Bmatrix}$$

A3. Magnetic-dipole matrix element

The magnetic-dipole matrix element $Z_1(av)$, which includes retardation, is given by

$$Z_1^{\mathrm{RF}}(av) = \langle -\kappa_a \,\|C_1\|\, \kappa_v\rangle \frac{6}{\alpha k}\int_0^\infty \mathrm{d}r\,\frac{(\kappa_a + \kappa_v)}{2}\,j_1(kr)\,[G_a(r)F_v(r) + F_a(r)G_v(r)] \quad \text{(A.8)}$$

$$Z_1^{(\mathrm{deriv})}(av) = \langle -\kappa_a \,\|C_1\|\, \kappa_v\rangle \frac{6}{\alpha k}\int_0^\infty \mathrm{d}r\,\frac{(\kappa_a + \kappa_v)}{2} \times [j_1(kr) - (kr)\,j_2(kr)]\,[G_a(r)F_v(r) + F_a(r)G_v(r)] \quad \text{(A.9)}$$

The magnetic-dipole matrix element $Z_1(av)$, without retardation, is given by

$$Z_1^{\mathrm{R}}(av) = \langle -\kappa_a \,\|C_1\|\, \kappa_v\rangle \frac{1}{\alpha}(\kappa_a + \kappa_v)\int_0^\infty \mathrm{d}r(r)\,[G_a(r)F_v(r) + F_a(r)G_v(r)] \quad \text{(A.10)}$$

$$Z_1^{(\mathrm{deriv})}(av) = Z_1^{\mathrm{R}}(av) \quad \text{(A.11)}$$

The nonrelativistic limit is different for transitions inside of one configurations, $n_a = n_v$, and transitions between different configurations, $n_a \neq n_v$. For the case $n_a = n_v$, we obtain

$$Z_1^{\mathrm{NR}}(av) = -\langle -\kappa_a \,\|C_1\|\, \kappa_v\rangle\,(\kappa_a + \kappa_v - 1)\frac{(\kappa_a + \kappa_v)}{2}\int_0^\infty \mathrm{d}r\,P_a(r)P_v(r) \quad \text{(A.12)}$$

where $P_a(r)$ is a nonrelativistic limit the large-component radial wave function $G_a(r)$. The case $n_a \neq n_v$ was considered in many papers for $1s^2\,{}^1S_0$- $1s2s\,{}^3S_1$ transitions (see, for example, ref. 27). The nonrelativistic limit in this case is proportional to Z^2, and for transitions with $l_a = l_v = 0$ the matrix element is given by [26]

$$Z_1^{\mathrm{NR}}(av) = -(\alpha Z)^2\sqrt{\frac{2}{3}}\left[\frac{3}{Z}\int_0^\infty \frac{1}{r}\,\mathrm{d}r\,P_a(r)P_v(r) + \frac{\omega^2}{2Z^2}\int_0^\infty r^2\,\mathrm{d}r\,P_a(r)P_v(r)\right] \quad \text{(A.13)}$$

Using hydrogenic wave functions, we find

$$M^{\mathrm{NR}}_{1s2s} = -(\alpha Z)^2\frac{16}{27\sqrt{3}}, \qquad M^{\mathrm{NR}}_{2s3s} = -(\alpha Z)^2\frac{2^4 23}{5^5} \quad \text{(A.14)}$$

A4. Electric-quadrupole matrix element

The electric-quadrupole matrix element $Z_2(av)$, which includes retardation, is given in velocity and length forms as

length gauge

$$Z_2(av) = \langle \kappa_a \| C_2 \| \kappa_v \rangle \frac{15}{k^2} \int_0^\infty \mathrm{d}r \{ j_2(kr) [G_a(r)G_v(r) + F_a(r)F_v(r)] + j_3(kr) \left(\frac{\kappa_a - \kappa_v}{3} [G_a(r)F_v(r) + F_a(r)G_v(r)] + [G_a(r)F_v(r) - F_a(r)G_v(r)] \right) \} \quad \text{(A.15)}$$

velocity form

$$Z_2(av) = \langle \kappa_a \| C_2 \| \kappa_v \rangle \frac{3}{k^2} \int_0^\infty \mathrm{d}r \{ 2 (j_1(kr) + j_3(kr)) [G_a(r)F_v(r) - F_a(r)G_v(r)] - \frac{\kappa_a - \kappa_v}{3} [-2j_3(kr) + 3j_1(kr)] [G_a(r)F_v(r) + F_a(r)G_v(r)] \} \quad \text{(A.16)}$$

The reduced matrix element for the derivative term is given by the following expressions:

length gauge

$$Z_2^{(\mathrm{deriv})}(av) = \langle \kappa_a \| C_2 \| \kappa_v \rangle \frac{15}{k^2} \int_0^\infty \mathrm{d}r [2j_2(kr) - (kr) j_3(kr)] [G_a(r)G_v(r) + F_a(r)F_v(r)] + \langle \kappa_a \| C_2 \| \kappa_v \rangle \frac{15}{k^2} \int_0^\infty \mathrm{d}r [(kr) j_2(kr) - 4j_3(kr)] \times \left[\frac{\kappa_a - \kappa_v}{3} [G_a(r)F_v(r) + F_a(r)G_v(r)] + [G_a(r)F_v(r) - F_a(r)G_v(r)] \right] \quad \text{(A.17)}$$

velocity form

$$Z_2^{(\mathrm{deriv})}(av) = \langle \kappa_a \| C_2 \| \kappa_v \rangle \frac{3}{k^2} \int_0^\infty \mathrm{d}r \{ [-8j_3(kr) + 2j_1(kr)] [G_a(r)F_v(r) - F_a(r)G_v(r)] - \frac{\kappa_a - \kappa_v}{3} [-5(kr) j_2(kr) + 8j_3(kr) + 3j_1(kr)] [G_a(r)F_v(r) + F_a(r)G_v(r)] \} \quad \text{(A.18)}$$

The nonrelativistic limit for the length and velocity forms of electric-quadrupole matrix element $Z_2(av)$ is equal to

length gauge

$$Z_2^{\mathrm{NR}}(av) = Z(av) = \langle \kappa_a \| C_2 \| \kappa_v \rangle \int_0^\infty \mathrm{d}r (r)^2 P_a(r) P_v(r) \quad \text{(A.19)}$$

velocity form

$$Z_2^{\mathrm{NR}}(av) = - \langle \kappa_a \| C_2 \| \kappa_v \rangle (\varepsilon_v - \varepsilon_a) \frac{\alpha}{k} \int_0^\infty \mathrm{d}r (r)^2 P_a(r) P_v(r) \quad \text{(A.20)}$$

The nonrelativistic limit for the derivative term of electric-quadrupole matrix element $Z_2^{(\mathrm{deriv})}(av)$ is equal to

length gauge

$$Z_2^{(\mathrm{deriv})}(av) = \langle \kappa_a \| C_2 \| \kappa_v \rangle 2 \int_0^\infty \mathrm{d}r (r)^2 P_a(r) P_v(r) \quad \text{(A.21)}$$

velocity form

$$Z_2^{(\mathrm{deriv})}(av) = -\langle \kappa_a \| C_2 \| \kappa_v \rangle \, (\varepsilon_v - \varepsilon_a) \, \frac{\alpha}{k} \int_0^\infty \mathrm{d}r (r)^2 P_a(r) P_v(r) \tag{A.22}$$

A5. Magnetic-quadrupole matrix element

The magnetic-quadrupole matrix element $Z_2(av)$, which includes retardation, is given as

$$Z_2(av) = \langle -\kappa_a \| C_2 \| \kappa_v \rangle \, \frac{30}{\alpha(k)^2} \int_0^\infty \mathrm{d}r \frac{(\kappa_a + \kappa_v)}{3} j_2(kr) \, [G_a(r) F_v(r) + F_a(r) G_v(r)] \tag{A.23}$$

The magnetic-quadrupole derivative matrix element $Z_2(av)$, which includes retardation, is equal to

$$Z_2^{(\mathrm{deriv})}(av) = \langle -\kappa_a \| C_2 \| \kappa_v \rangle \, \frac{30}{\alpha(k)^2} \int_0^\infty \mathrm{d}r \frac{(\kappa_a + \kappa_v)}{3} \, [2 j_2(kr) - (kr) j_3(kr)] \times [G_a(r) F_v(r) + F_a(r) G_v(r)] \tag{A.24}$$

The nonrelativistic limit for the magnetic-quadrupole matrix element $Z_2(av)$ is

$$\frac{1}{2} Z_2^{(\mathrm{deriv})\mathrm{NR}}(av) = Z_2^{\mathrm{NR}}(av) = -\langle -\kappa_a \| C_2 \| \kappa_v \rangle \, \frac{\kappa_a + \kappa_v}{3} \, (\kappa_a + \kappa_v - 2) \int_0^\infty \mathrm{d}r (r) P_a(r) P_v(r) \tag{A.25}$$

where $P_a(r)$ is a nonrelativistic limit of the large-component radial wavefunction $G_a(r)$.